Geochemistry, Geophysics, Geosystems

RESEARCH ARTICLE
10.1029/2020GC009507

Zircon and Melt Extraction From a Long-Lived and Vertically Extensive Magma System Underneath Ilopango Caldera (El Salvador)

A. Cisneros de León[1], A. K. Schmitt[1], S. Kutterolf[2], J. C. Schindlbeck-Belo[1,2], W. Hernández[3], K. W. W. Sims[4], J. Garrison[5], L. B. Kant[4], B. Weber[6], K.-L. Wang[7,8], H.-Y. Lee[7], and R. B. Trumbull[9]

[1]Institut für Geowissenschaften, Universität Heidelberg, Heidelberg, Germany, [2]GEOMAR Helmholtz Centre for Ocean Research Kiel SFB574, Kiel, Germany, [3]Observatorio Ambiental, Ministerio de Medio Ambiente y Recursos Naturales, San Salvador, El Salvador, [4]Department of Geology and Geophysics, University of Wyoming, Laramie, WY, USA, [5]Department of Geosciences and Environment, California State University, Los Angeles, CA, USA, [6]Departamento de Geología, Centro de Investigación Científica y de Educación Superior de Ensenada, Ensenada, BC, Mexico, [7]Institute of Earth Sciences, Academia Sinica, Taipei, Taiwan, [8]Department of Geosciences, National Taiwan University, Taipei, Taiwan, [9]GFZ German Research Centre for Geosciences, Potsdam, Germany

Abstract The Tierra Blanca (TB) eruptive suite comprises the last four major eruptions of Ilopango caldera in El Salvador (≤45 ka), including the youngest Tierra Blanca Joven eruption (TBJ; ~106 km^3): the most voluminous event during the Holocene in Central America. Despite the protracted and productive history of explosive silicic eruptions at Ilopango caldera, many aspects regarding the longevity and the prevailing physicochemical conditions of the underlying magmatic system remain unknown. Zircon ^{238}U-^{230}Th geochronology of the TB suite (TBJ, TB2, TB3, and TB4) reveals a continuous and overlapping crystallization history among individual eruptions, suggesting persistent melt presence in thermally and compositionally distinct magma reservoirs over the last ca. 80 kyr. The longevity of zircon is in contrast to previously determined crystallization timescales of <10 kyr for major mineral phases in TBJ. This dichotomy is explained by a process of rhyolitic melt segregation from a crystal-rich refractory residue that incorporates zircon, whereas a new generation of major mineral phases crystallized shortly before eruption. Ti-in-zircon temperatures and amphibole geothermobarometry suggest that rhyolitic melt was extracted from different storage zones of the magma reservoir as indicated by distinct but synchronous thermochemical zircon histories among the TB suite eruptions. Zircon from TBJ and TB2 suggests magma differentiation within deeper and hotter parts of the reservoir, whereas zircon from TB3 and TB4 instead hints at crystallization in comparatively shallower and cooler domains. The assembly of the voluminous TBJ magma reservoir was also likely enhanced by cannibalization of hydrothermally altered components as suggested by low-δ^{18}O values in zircon (+4.5 ± 0.3‰).

Plain Language Summary The collapse of a volcano edifice into its shallow magma chamber can produce one of the most dangerous single events in nature, known as a caldera-forming eruption. The TBJ eruption in El Salvador is of this kind and occurred around 1,500 years ago, having a profound impact on Maya societies. Because of this, it is crucial to understand the inner workings of caldera-forming eruptions to assess volcanic risks and their mitigation. Beneath Ilopango caldera, the micrometer-sized radioisotopically datable mineral zircon grew within different storage levels of a silica-rich magma reservoir suggesting continuous melt presence for up to ca. 80,000 years prior to eruption. The time information given by zircon contrasts with that extracted from other, more abundant minerals from the same rocks (<10,000 years). We explain this time difference between coexisting minerals by the ability of melt to carry along small zircon crystals, whereas coeval, larger, and more abundant minerals are left behind in the partially solidified portion of the magma reservoir. Once the segregated melt coalesced in a shallower and dominantly liquid magma chamber, major minerals resumed crystallization shortly before eruption. In addition, this new magma incorporated parts of older magmatic rocks from preceding volcanic cycles, thus generating even larger magma volumes.

Key Points:

- U-Th zircon ages for the last four explosive eruptions of Ilopango caldera reveal a long-lived magma reservoir (>80 kyr)
- Contrasting residence times for major minerals and zircon suggest extraction of zircon along with evolved melt from crystal residue
- Melt extraction from vertically extensive, thermally zoned magma reservoir

Supporting Information:

Supporting Information may be found in the online version of this article.

Correspondence to:

A. Cisneros de León,
cisneros.deleon@outlook.de

Citation:

Cisneros de León, A., Schmitt, A. K., Kutterolf, S., Schindlbeck-Belo, J. C., Hernández, W., Sims, K. W. W., et al. (2021). Zircon and melt extraction from a long-lived and vertically extensive magma system underneath Ilopango caldera (El Salvador). *Geochemistry, Geophysics, Geosystems*, *22*, e2020GC009507. https://doi.org/10.1029/2020GC009507

Received 4 NOV 2020
Accepted 14 FEB 2021

1. Introduction

Caldera-forming silicic volcanic eruptions are among the most violent and devastating events on Earth (Miller & Wark, 2008; Newhall et al., 2018). The release of tens to thousands of cubic kilometers of magma producing widespread fallout and ground-hugging hot and turbulent pyroclastic flows are potential threats to life within large areas from the source (>100 km; Koch & Mclean, 1975; Wilson et al., 1995), while emissions of climate-forcing gases can have a global impact (Self & Blake, 2008; Sheets, 2015; Brenna et al., 2020, 2021). One such devastating eruption was the variably dated 431–545 CE Tierra Blanca Joven (TBJ) eruption (~106 km^3) from Ilopango caldera in El Salvador, Central America (Dull et al., 2019; Pedrazzi et al., 2019; Smith et al., 2020). During this eruption, densely populated Maya settlements were buried under pyroclastic deposits (~40,000–80,000 casualties; Dull et al., 2019; Hart & Steen-McIntyre, 1983) causing a profound reorganization of the Maya society at political, economic, and demographic levels (Dull et al., 2001, 2019; Sheets, 2015). Despite the extreme hazards associated with Ilopango caldera, and very recent signs of silicic magmatic activity (in 1880 CE; Richer et al., 2004), the frequency of precursor eruptions to the TBJ event as well as the timescales and mechanisms of assembly and storage of eruptible magma has not been adequately studied.

Over the past decade, traditional concepts of long-lived single magma bodies feeding voluminous eruptions have been superseded by models invoking rapid assembly of magma by merging of discrete magma batches (Bégué et al., 2014; Cashman & Giordano, 2014; Wotzlaw et al., 2014, 2015) or by remobilization of crystal-rich ("mushy") or subsolidus intrusions that have accumulated at shallow depth underneath polycyclic caldera systems prior to eruption (Annen et al., 2006; Annen & Sparks, 2002; Bergantz et al., 2015; Ellis et al., 2017; Sliwinski et al., 2017). Ilopango caldera is an ideal location for investigating these processes as it underwent four major eruptions of evolved magma (rhyolitic-dacitic) over the last <57 kyr (Rose et al., 1999), all of which contain zircon as an accessory mineral. Previous studies (Garrison et al., 2012) have provided evidence from U-series geochronology that major minerals in TBJ crystallized rapidly before the eruption. Zircon can be used as a complementary chronometer for the assembly of such voluminous eruptible magma bodies, and compared to major minerals, it has the advantage that individual crystal domains can be directly dated. Its potential as an absolute chronometer (U-series and U-Pb) can be further enhanced when combined with chemical and isotopic compositions obtained from the same dated volume of crystals (e.g., trace elements, Ti-in-zircon temperatures, $\delta^{18}O$). This can offer time-integrated insights into magma chamber conditions and dynamics at various stages during the reservoir evolution (Claiborne et al., 2010; Reid & Vazquez, 2017; Schmitt, 2011; Vazquez & Reid, 2002).

In order to understand temporal changes in magmatic processes and storage conditions prior, during, and after caldera-forming eruptions, we investigated the last four major rhyolitic-dacitic explosive events from Ilopango caldera in El Salvador (TB suite) employing zircon petrochronology (^{238}U-^{230}Th and U-Pb geochronology combined with O-isotope and trace element geochemistry). The zircon data are supported by whole-rock $^{87}Sr/^{86}Sr$, $^{144}Nd/^{143}Nd$, ^{238}U-^{230}Th isotopes, whole-rock, glass, and amphibole thermobarometry.

2. Geological Background

Silicic magmatism from Ilopango caldera in central El Salvador is ultimately caused by the subduction of the Cocos slab beneath the Caribbean plate (Carr, 1984). The Cocos-Caribbean convergent margin has produced at least ~39 silicic to mafic volcanic centers (~807 volcanic vents; Carr, 2017) including several calderas and voluminous composite volcanoes which together form the Central American Volcanic Arc (CAVA; Carr et al., 2003). The CAVA extends >1,200 km parallel to the Pacific coast from the southeasternmost limits of Mexico to Panama (Carr et al., 2003; Kutterolf et al., 2008). Today, Ilopango caldera consists of an ~11 × 14 km E-W elongated collapse structure filled by a lake of ~235 m water depth (Figure 1a; Sánchez, 2015). It is partially encroached by the urban spread of the San Salvador Metropolitan area (~1.7 million inhabitants; Figure 1b; Mann et al., 2004).

The oldest known eruptive products of Ilopango caldera are dated at ca. 2 Ma (K-Ar; Zaragoza ignimbrite; Lexa et al., 2011; Suñe-Puchol et al., 2019b). The most recent magmatic activity occurred during historic times (1879–1880 CE); this event comprised dacitic domes that grew within the caldera lake (Islas Quemadas; 0.13 km^3; Newhall & Dzurisin, 1988). Between these two bracketing events, was a series of large to

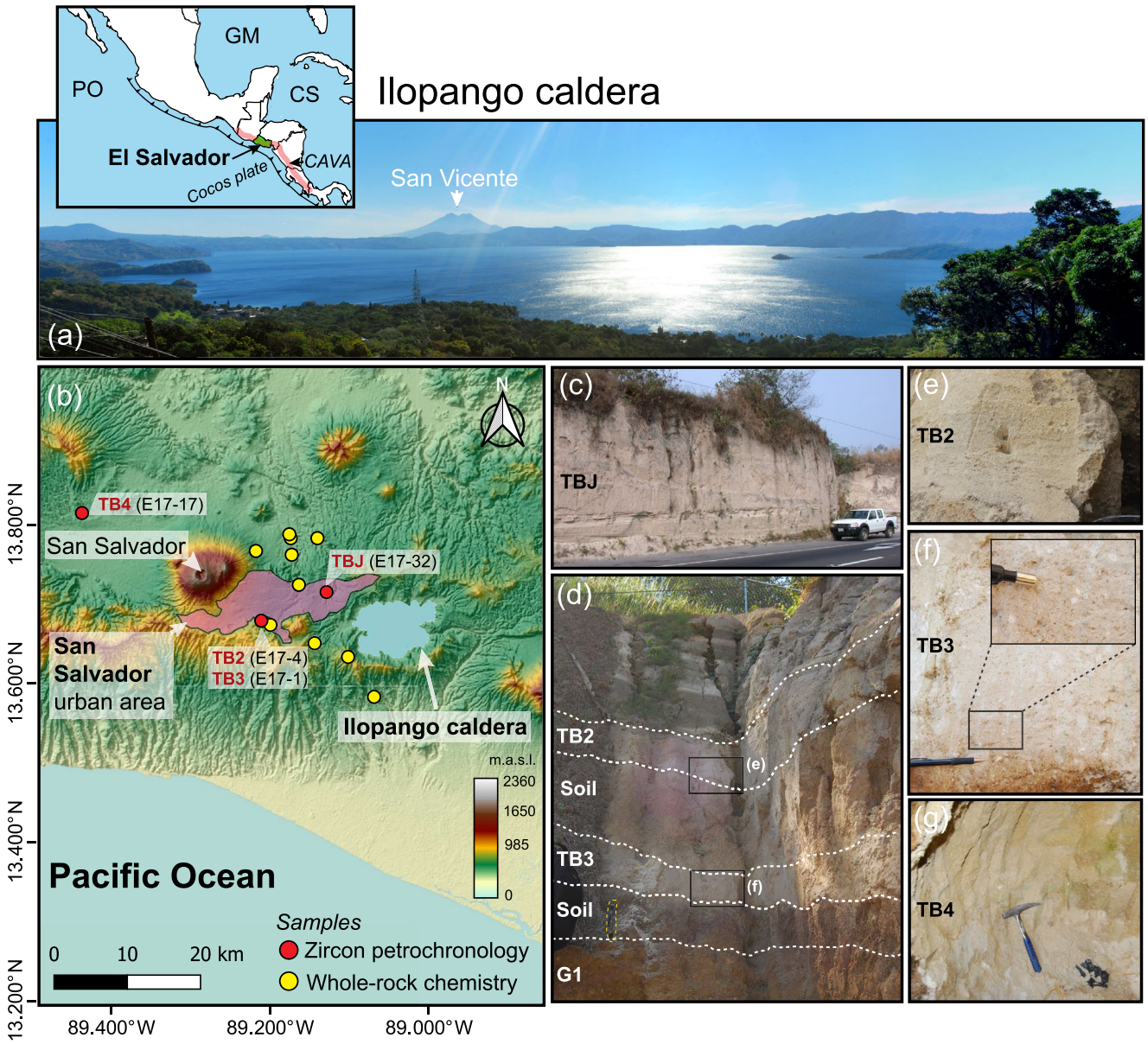

Figure 1. Sample locations and field photographs showing outcrops from the TB eruption suite (a) Ilopango Lake panorama. Inset shows regional tectonic setting; (b) Digital elevation model (DEM) with sample locations. Samples from which zircon was separated are in red, whereas those used only for geochemical analysis are in yellow. DEM information was obtained from USGS; (c) TBJ ignimbrite deposit; (d) TB2 and TB3 fall deposits separated by a layer of soil; (e) TB2 fall deposit close-up showing pyroclastic component textures; (f) TB3 fall deposit close-up showing pyroclastic component textures including accretionary lapilli; (g) Distal fall TB4 deposit.

medium sized explosive eruptions grouped into at least three eruptive cycles that include, from oldest to youngest, the Comalapa (ca. 1.78–1.34 Ma), Altavista (ca. 918–257 ka), and Tierra Blanca (<57 ka) eruption suites (Kutterolf et al., 2008; Pedrazzi et al., 2019; Rose et al., 1999; Suñe-Puchol et al., 2019a, 2019b).

The TB suite comprises, from oldest to youngest, the TB4, TB3, TB2, and TBJ events, which tapped rhyolitic to dacitic magma (Hernández et al., 2010; Kutterolf et al., 2008a, 2008b; Pedrazzi et al., 2019). TBJ (~106 km^3) and TB4 (~36 km^3) stand out as the most voluminous eruptions among the TB suite, with deposits extending to the Pacific Ocean (Dull et al., 2019; Kutterolf et al., 2008; Mehringer et al., 2005; Schindlbeck et al., 2018). Although radioisotopic dates for TB4, TB2, and TB3 were lacking prior to this study, stratigraphic position implies an age of <57 ka for TB4 (Rose et al., 1999), whereas sedimentation rates suggest an apparent age of ca. 36 ka for the same eruption (Kutterolf et al., 2008). The TBJ eruption

was radioisotopically defined at ca. 500–545 CE (Dull, et al., 2019, 100 AMS dates) and most recently dated to 431 ± 2 CE (Smith et al., 2020, 11 AMS dates), both dates obtained by the ^{14}C method. Deposits from the TBJ eruption are interpreted to have resulted from a complex phreatoplinian event (Houghton et al., 2015; Pedrazzi et al., 2019). The TBJ eruptive sequence comprises a thick (~60 m) proximal succession of fallout, ignimbrite, and surge deposits subdivided into at least eight subunits of dacitic to rhyolitic compositions (Pedrazzi et al., 2019). Pumice with a sporadically intermingled glass of basaltic composition (Hart & Steen-McIntyre, 1983; Pedrazzi et al., 2019) may represent a parental magma that could have been responsible for triggering the eruption (Garrison et al., 2012; Richer et al., 2004). Overall, TBJ eruptive products contain up to 15% phenocrysts supported in a highly stretched and highly vesicular glassy matrix. The previously reported mineral assemblage mainly consists of plagioclase > hornblende > pyroxene > Fe-Ti oxides, apatite, and zircon (Garrison et al., 2012; Pedrazzi et al., 2019). A similar assemblage has also been reported for the older TB2, TB3, and TB4 tephras (Kutterolf et al., 2008). Although little studied, TB2, TB3, and TB4 tephras are also thought to represent products of Plinian/phreatoplinian explosive events (Lexa et al., 2011). The TB2 and TB3 tephras are both the result of small phreatoplinian eruptions of dacitic magma. The TB2 fallout deposits comprise white to beige pumice deposits, with abundant polymineralic crystal clusters of amphibole, pyroxene, magnetite, and plagioclase. The TB3 deposits consist of fine ash with variable amounts of accretionary lapilli and fine to coarse pyroclastic surge deposits, whereas both deposits have similar estimated volumes of 1–5 km^3 (Lexa et al., 2011). The TB4 proximal rhyolitic tephra consists of moderately sorted coarse pumice (~1–5 cm) fallout deposits with thin layers of fine ash at the bottom and top. Its thickness at proximal locations can reach ~7 m (Hernández, 2004; Lexa et al., 2011).

Recent Bouguer gravity geophysical investigations suggest that magma ascent and accumulation beneath Ilopango caldera occurs within a shallow, highly fractured, and hydrothermally altered plumbing system that is controlled by a complex array of dextral strike-slip faults with dominant E-W strike of the El Salvador Fault Zone (ESFZ; Corti et al., 2005; Saxby et al., 2016). In a first reconnaissance study of TBJ ash in archeological materials, ^{238}U-^{230}Th zircon dating from TBJ pumice clasts suggested timescales of <30 ka for magma storage prior to eruption (Coffey et al., 2014), whereas ^{238}U-^{230}Th mineral-whole-rock/glass isochrons (e.g., magnetite, amphibole, and pyroxene) indicated much shorter timescales of <10,000 years for crystallization and magmatic differentiation (Garrison et al., 2012). Magma genesis at Ilopango caldera has been modeled by pure fractional crystallization of parental basaltic andesite, but the same study documented differences in whole-rock $^{143}Nd/^{144}Nd$, $^{87}Sr/^{86}Sr$, and $^{207}Pb/^{206}Pb$ isotope values that indicate contributions from heterogeneous magmatic sources and/or country rocks (Garrison et al., 2012).

3. Sampling and Analytical Methods

3.1. Samples

Samples from the entire TB suite were collected from proximal, medial, and distal locations where clear stratigraphic control exists (Figure 1b). Samples from which zircon crystals were separated are described here, whereas other sample descriptions are presented in Table S1. The TBJ composite pumice sample (E17-32) was collected from a proximal location ~3 km from the caldera lake and corresponds to a massive ignimbrite flow unit consisting of rare lapilli pumice (<5 cm) and lithic fragments (<1 cm) supported by a massive white-beige ash matrix (<250 μm; Figure 1c). TB2 (E17-4) and TB3 (E17-1) are composite pumice samples that were both collected from the same outcrop ~18 km from the caldera (Figure 1d). TB2 and TB3 deposits are separated by an ~60 cm thick soil horizon. TB2 tephra occurs as an ~35 cm thick layer constituted by inversely graded pumice and ash fall with medium to coarse ash at the lower part and fine to medium lapilli at the uppermost ~10 cm (Figure 1e); TB3 tephra is an ~40 cm thick layer with an erosive contact at the base (Figure 1f). It is composed dominantly of white to beige and medium to fine ash with pumice lapilli enrichment at the top that included fine ash pockets. Below TB3 and separated by a soil horizon is a >1 m thick scoria layer sourced from San Salvador volcano (G1). TB4 distal tephra was collected ~45 km from the source from an ~1.5 m thick layer composed of coarse ash with few fine pumice lapilli (Figure 1g).

3.2. Methods

Samples from the TB suite were selected for zircon ^{238}U-^{230}Th disequilibrium and U-Pb dating as well as for zircon trace element and oxygen isotope analysis (only TBJ zircon). Zircon crystals were analyzed in the same dated domains on unsectioned faces for all samples (providing crystallization ages of the outermost crystal face) and also from exposed crystal interiors of TBJ zircon. In most cases zircon crystal separates presented adhering glass, suggesting suspension in melt prior to eruption. Zircon analyses were carried out on a CAMECA IMS 1280-HR secondary ion mass spectrometer (SIMS) at Heidelberg University, Germany, Tables S2–S5). Whole-rock chemical analyses were performed at the German Research Centre for Geosciences (GFZ) using a PANalytical AXIOS Advanced wavelength-dispersive spectrometer (Table S6), whereas major and trace elements, glass shard, and mineral compositions were collected using an electron microprobe analysis (EMPA) at GEOMAR—Helmholtz-Center for Ocean Research Kiel and by Laser Ablation Inductively Coupled Plasma-Mass Spectrometry (LA-ICP-MS) at Institute of Earth Sciences, Academia Sinica in Taipei (Taiwan; Tables S7 and S8). Whole-rock Sr-Nd isotope determinations were carried out at Departamento de Geología, Centro de Investigación Científica y de Educación Superior de Ensenada (CICESE) in the state of Baja California (Mexico), whereas whole-rock U-series were determined using a ThermoFisher Neptune ICP-MS multicollector at the University of Wyoming (UWYO, USA; Table S9). Detailed methodologies are presented in Text S1.

4. Results

4.1. Petrography

All samples from the TB suite are mineralogically and texturally similar, and our petrographic findings for TBJ tephra are relatively similar to previously reported petrographic descriptions (e.g., Garrison et al., 2012; Pedrazzi et al., 2019). Over the entire TBJ eruptive sequence, pumice is uniformly crystal-poor (<15%) and composed mainly of glass with highly stretched vesicles (Figure S1). In addition, TBJ pumice locally contains irregular glomerocrystic enclaves that account for 30–40% of the total crystal content of pumice clasts. These glomerocrystic enclaves contain large and mostly rounded vesicles and large phenocrysts (~200–1,000 μm; Figure S1) composed of plagioclase and amphibole with minor magnetite, apatite, zircon, and sporadic orthopyroxene, ilmenite, and quartz. TBJ crystals scattered in the pumice matrix are similar to the mineralogy of glomerocrysts. Plagioclase commonly presents oscillatory zonation and, in some cases, preserves evidence of complex textures (e.g., sieved, discordant zonation, and corroded rims). Amphibole often has pristine rims, but marginal replacement by fine-grained oxide-rich intergrowths is present in some crystals. Without exception, magnetite from TBJ is characterized by abundant inclusions or marginally intergrown apatite and zircon. Zircon can also be found as inclusions in most of the phenocryst assemblage. TB3 tephra consists of a crystal assemblage that comprises <10% of the total rock volume and includes plagioclase, amphibole, magnetite, quartz, zircon, and apatite. Phenocrysts are scattered randomly in a glassy and highly stretched vesicular matrix that texturally resembles that of TBJ (Figure S2). Rare glomerocrystic enclaves have higher crystallinity (~40–50%) and are composed mainly of large plagioclase crystals, interstitial orthopyroxene, and magnetite supported in a glassy matrix. Lithic inclusions are pumiceous with a highly altered matrix containing plagioclase, amphibole, quartz, and pyroxene. Large monomineralic plagioclase glomerocrysts (>2,000 μm) are present in some pumice clasts. These glomerocrysts are likely associated with the remobilization of intrusive portions of the magma chamber prior to the eruption, but because of their relative scarcity, they neither contribute significantly to the whole-rock chemistry nor to the zircon separates. TB4 pumice clasts are crystal-poor (<5%) with an assemblage dominated by large plagioclase crystals (~200–1,000 μm) scattered around the vesicle-rich glassy matrix. Amphibole and quartz crystals are rare, whereas pyroxene crystals were absent.

4.2. Whole-Rock and Glass Chemistry

Whole-rock analyses of major elements from the entire TB suite fall within the calk-alkaline series. Except for one TBJ analysis from the uppermost flow unit with ~63 wt % SiO_2 content (recalculated anhydrous), the rest of the samples are in the range between ~69 and 73 wt % SiO_2. TB4 shows similar SiO_2 contents as TBJ, and both fall mostly in the field of rhyolite on the total alkali-silica diagram (Figure 2a). TB2 and TB3

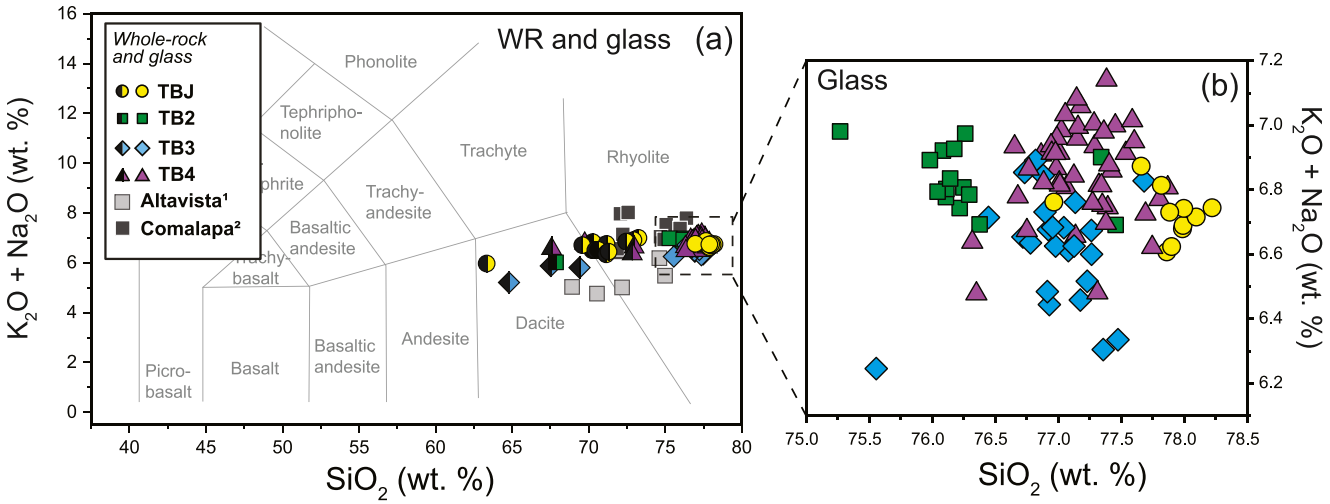

Figure 2. Total Alkali-Silica (TAS) classification diagram after Le Maitre et al. (1989) and glass major element geochemistry of the TB eruption suite. Whole symbols are glass compositions; divided symbols represent whole-rock samples. Geochemical data from older Ilopango units known as Altavista and Comalapa suites are from Suñe-Puchol et al. (2019a, 2019b).

exhibit slightly lower SiO_2 contents than TB4, ranging from ~65 to ~69 wt %, and are classified as dacite. Glass analyses from the entire TB eruption suite correspond to the compositional field of rhyolite (Figure 2a). However, subtle differences in glass compositions distinguish the four eruptions chemically. For instance, TBJ glass has on average the highest SiO_2 contents, whereas the preceding TB2 eruption shows glass compositions with the lowest SiO_2 contents of the TB suite (Figure 2b). TB3 and TB4 overlap in SiO_2 abundances that are intermediate with respect to TB2 and TBJ, but display on average a slightly contrasting behavior in total alkali content. Trace elements (e.g., Sr) display well-defined negative correlations with SiO_2 (Figure S3).

4.3. Whole-Rock Sr-Nd and U-Th Isotopes

Whole-rock Sr-Nd isotope ratios for the TB eruption suite show a relatively restricted range in both isotope systems. Measured ratios of $^{87}Sr/^{86}Sr$ varies from 0.703808 ± 9 to 0.703840 ± 9, whereas $^{144}Nd/^{143}Nd$ ranges from 0.512975 ± 12 to 0.513000 ± 7 (2σ). The entire data set shows a positive trend in $^{144}Nd/^{143}Nd$ versus $^{87}Sr/^{86}Sr$ that overlaps with isotope compositions from other volcanoes in El Salvador (Figures 3a and 3b).

All analyzed samples are characterized by $(^{230}Th)/(^{238}U) > 1.0$, with ^{230}Th excesses ranging from ~1% (TB4) up to ~83% (TB2; Figure 3c; all samples were corrected for time since eruption using the estimated eruption age from ^{238}U-^{230}Th zircon crystallization ages; Table 1). Excesses in ^{230}Th correlate negatively with $^{87}Sr/^{86}Sr$ (Figure 3d). The oldest TB4 tephra shows a similar initial $(^{230}Th)/(^{238}U)_0$ as the youngest TBJ, both plotting near the equiline.

4.4. U-Th and U-Pb Zircon Crystallization Ages

Zircon crystals rims (pristine surfaces) from eruptions TBJ, TB2, TB3, and TB4 were analyzed in order to retrieve their age spectra and to estimate eruption age based on Bayesian statistics after Keller et al. (2018) for the undated TB2, TB3, and TB4 eruptions (Table 1). Zircon crystal morphologies from the TB suite show some differences (Figure 4). TBJ zircon is characterized by rounded edges with a large proportion of crystals exhibiting intense resorption surfaces, although well-faceted prismatic zircon crystals are also present (Figures 4a and 4b). TB2 and TB3 zircon crystals are similar in shape, showing typically elongated forms with well-defined crystal faces and occasional semi-rounded edges (Figures 4c and 4d). TB3 zircon is on average much larger than zircon from the other samples, usually >100 μm in length. TB4 zircon is somewhat different from the rest. Although it shows elongated shapes in a few cases, the morphology is dominated by more equant and euhedral shapes and also smaller sizes (<100 μm; Figure 4e). CL imaging of TBJ zircon interiors

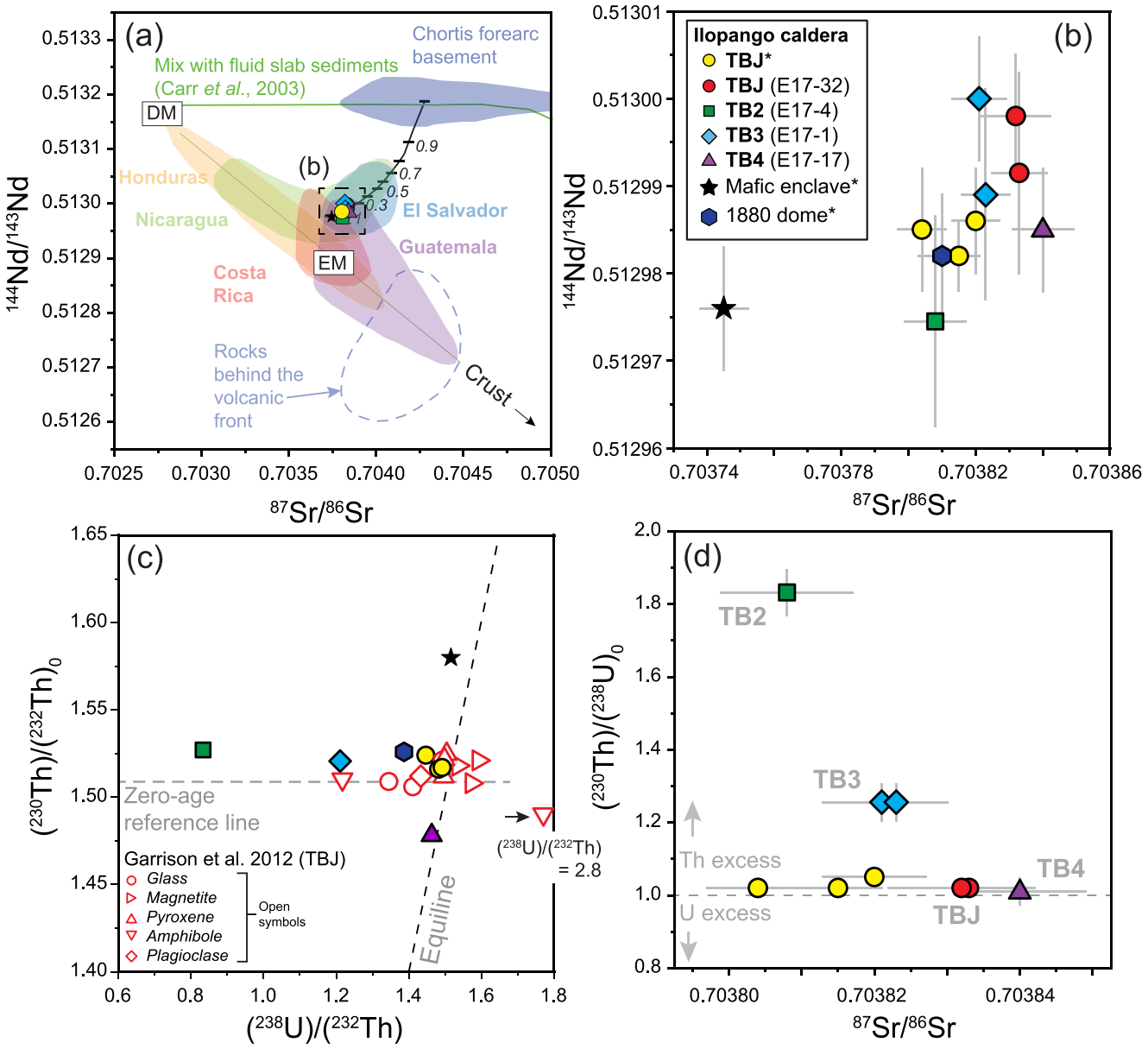

Figure 3. Whole-rock Sr-Nd and U-series isotope diagrams for Ilopango caldera rocks. (a) $^{87}Sr/^{86}Sr$ versus $^{144}Nd/^{143}Nd$ diagram showing typical compositions for other CAVA rocks. Modified from Scarlato et al. (2017) and Garrison et al. (2012); The solid black line represents a modeled mixing curve between the mantle array and 5% melt of the forearc basement of the Chortis Block; small italicized numbers represent the proportion of Chortis block crust in the mixture. The dashed line represents the sediment-mantle mixing model of Feigenson and Carr (1986). EM = Enriched MORB source, DM = Depleted MORB source; (b) $^{87}Sr/^{86}Sr$ versus $^{144}Nd/^{143}Nd$ diagram showing variations among TB eruption suite samples; (c) Initial $(^{230}Th)/(^{238}U)_0$ equiline diagram showing samples from TB eruption suite; color in open symbols indicate different TBJ samples; Samples were age-corrected based on eruption maxima obtained from zircon U-Th crystallization ages (see Table 1); Errors bars in (c) omitted for clarity; (d) $(^{230}Th)/(^{238}U)_0$ versus $^{87}Sr/^{86}Sr$ diagram. * = data from Garrison et al. (2012).

frequently reveals resorbed antecrystic domains; these mostly form cores and are mantled by juvenile overgrowths, but usually exhibit similar CL intensities (Figure 5a). In some cases, however, cores are distinctively darker and have relatively higher U content. Both core and mantle domains typically display oscillatory zonation and abundant glass and mineral inclusions (e.g., magnetite, ilmenite, and apatite; Figure 5a).

Zircon from TBJ displays U-Th rim crystallization ages (n = 38) that range from 1 $^{+9}/_{-9}$ ka (1σ) to secular equilibrium (ages >350 ka, unresolvable by U-Th dating methods; Figure 4a). Most TBJ zircon crystallization ages fall within a timespan <100 ka, in which the two youngest zircon rim ages overlap within the error of the radiocarbon eruption age of ca. 431–545 CE. The age probability-density function (PDF) indicates a

Table 1
Stratigraphic Summary of the TB Eruption Suite From Ilopango Caldera and Respective Radioisotopic Ages

Formation	Eruption	Glass composition	Bulk composition	Volume	Age	Dating method
San Salvador Fm.	TBJ	Rhyolite	Rhyolite	~106 km^3	**431 CE**	^{14}C[a]
					540 CE	^{14}C[b]
					0 ka	^{238}U-^{230}Th zircon[c,*]
	TB2	Rhyolite	Dacite	<5 km^3	**8.3 ± 6.4 ka**	^{238}U-^{230}Th zircon[c,*]
	TB3	Rhyolite	Dacite	<5 km^3	**16 ± 7.8 ka**	^{238}U-^{230}Th zircon[c,*]
	TB4	Rhyolite	Rhyolite	~36 km^3	**45 ± 4.6 ka**	^{238}U-^{230}Th zircon[c,*]
					ca. 36 ka	Sedimentation rates[d]

Note. preferred eruption ages are in bold.
[*]Maximum eruption age based on U-Th zircon crystallization Bayesian statistics following Keller et al. (2018). [a]Smith et al. (2020). [b]Dull et al. (2019). [c]This study. [d]Kutterolf et al. (2008).

polymodal distribution with major crystallization peaks resolved by the unmixing age model of Sambridge and Compston (1994) at ca. 21 $^{+6}/_{-6}$ ka, 56 $^{+12}/_{-14}$ ka, 111 $^{+25}/_{-33}$ ka, and at secular equilibrium (accounting for ~40% of the crystals analyzed). Crystal interiors of TBJ zircon (n = 72) show an age range from 10 $^{+5}/_{-5}$ ka to secular equilibrium (~38% of the crystals analyzed), with most dates also concentrating within <100 ka (Figure 4b). Major age peaks occur at ca. 15 $^{+4}/_{-4}$ ka, 33 $^{+4}/_{-4}$ ka, 54 $^{+4}/_{-4}$ ka, 91 $^{+10}/_{-11}$ ka, and at secular equilibrium. Intra-grain zircon age differences between core and mantle vary between 0.7 and 67 kyr. Zircon rim ages from TB2 eruption (n = 52) range from 8 $^{+10}/_{-9}$ ka to secular equilibrium (~11% of the crystals analyzed), although most zircon crystallized at <100 ka (Figure 4c). The age distribution peaks for TB2 occur at ca. 22 $^{+3}/_{-3}$ ka, 63 $^{+23}/_{-29}$ ka, and at 162 $^{+32}/_{-47}$ ka. TB3 zircon (n = 30) shows an age spectrum ranging from 19 $^{+5}/_{-5}$ ka to secular equilibrium (~3% of the crystals analyzed) with modes at ca. 30 $^{+3}/_{-3}$ ka, and 213 $^{+34}/_{-50}$ ka (Figure 4d). In contrast to the younger eruptions, most TB3 zircon ages are <80 ka, although a small group of ages cluster between ca. 200 ka and <350 ka. Zircon crystals from TB4 eruption (n = 48) exhibit an age range from 41 $^{+13}/_{-11}$ ka to secular equilibrium (~6% of the crystals analyzed), showing a major peak crystallization episode at 60 $^{+4}/_{-4}$ ka, and two minor peaks at 90 $^{+7}/_{-8}$ ka and secular equilibrium (Figure 4e). Interestingly, all samples of the TB suite display a conspicuous minimum in zircon crystallization ages between ca. 100 and 160 ka.

U-Pb disequilibrium-corrected ages for TBJ zircon interiors (from grains at secular equilibrium) yielded ages ranging from 266 ± 34 ka to 2.26 ± 0.74 Ma (Figure 5b). This covers the same timescale as the known eruptive history of Ilopango caldera (Hernández & Jicha, 2019; Lexa et al., 2011; Suñe-Puchol et al., 2019a). Major age distribution peaks occur at ca. 310 and 580 ka preceding large eruptions of the Altavista suite. Two early Miocene grains of 16.7 ± 1.5 and 19.8 ± 1.6 Ma are interpreted as xenocrysts derived from country-rock.

4.5. Amphibole Geothermobarometry

Amphibole crystals from the entire TB suite were analyzed in order to estimate crystallization temperature and pressure conditions following the approach of Ridolfi et al. (2010; Figure 6a). TB4 amphibole ranges in temperature from 913 to 941 °C (average = 925 ± 11 °C; 1s.d.; n = 3) and pressures from 284 to 426 MPa (average = 353 ± 57 MPa; 1s.d.). Similar temperatures and pressures were obtained for TBJ amphibole, ranging from 806 to 951 °C (average = 894 ± 53 °C; n = 8) and from 117 to 349 MPa (average = 262 ± 86 MPa; 1s.d.). TB3 and TB2 amphibole indicates on average equilibration under colder and shallower conditions, although there is some overlap in the values from all eruptions. TB3 amphibole geothermobarometry yield temperatures from 820 to 900 °C (average = 839 ± 22 °C; n = 9) and pressures from 128 to 259 MPa (average = 156 ± 37°MPa; 1s.d.), whereas TB2 amphibole from 822 to 893 °C (average = 859 ± 15 °C; 1s.d.; n = 56) and from 86 to 214 MPa (average = 127 ± 18 MPa; 1s.d.).

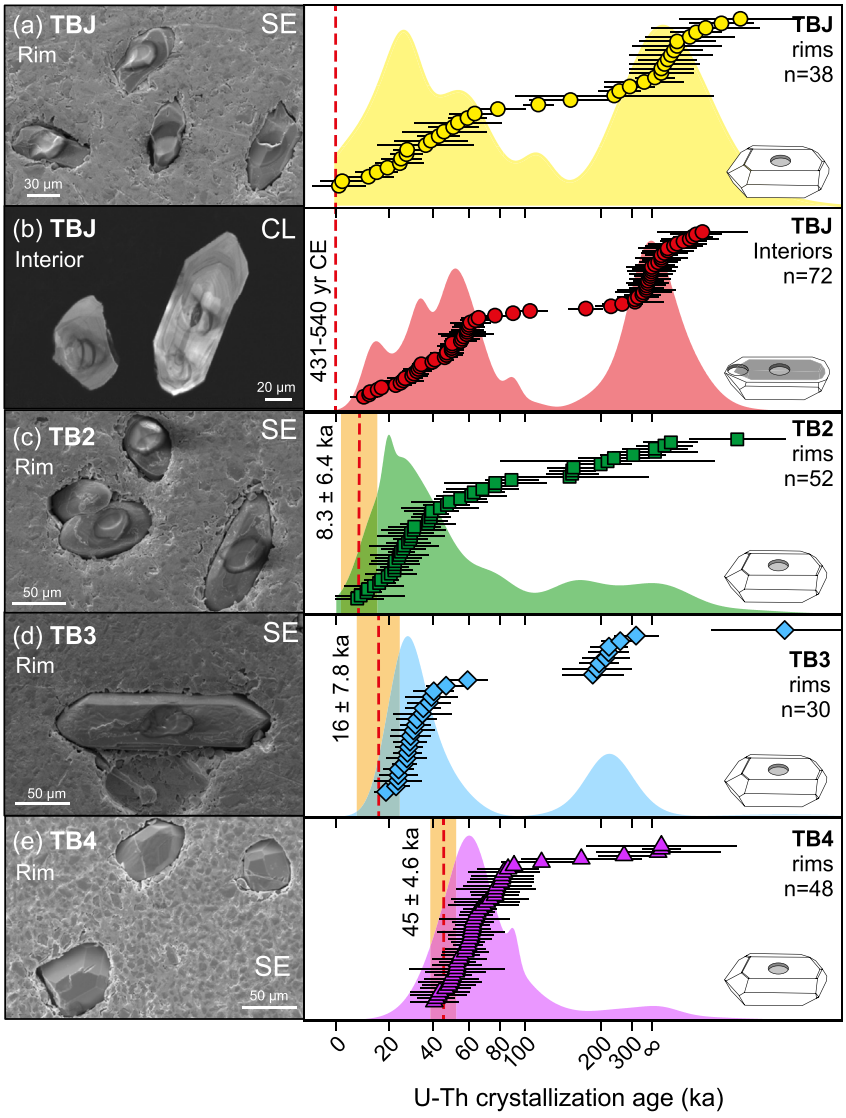

Figure 4. Ranked-order plots of model ^{238}U-^{230}Th zircon crystallization ages with examples of crystal morphology and internal structure from secondary electron (SE) and cathodoluminescence (CL) imaging. The PDF was constructed based on two-point isochron slopes; corresponding model ages are plotted on the *x* axis. Red vertical dashed lines represent eruption estimates based on the model of Keller et al. (2018) for ^{238}U-^{230}Th zircon crystallization age populations and in the case of TBJ on the known eruption age of 431–545 CE.

4.6. Ti-In-Zircon Temperatures

Zircon crystallization temperatures were calculated following the Ti-in-zircon calibration of Ferry and Watson (2007); details of the Ti-in-zircon thermometry regarding assumptions of $a\mathrm{TiO_2}$ and $a\mathrm{SiO_2}$ are presented in Text S1). Zircon crystallization temperatures from TBJ are variable over the ca. 1.2 Myr crystallization history (Figure 6b). These range between 838 and 689 °C (average = 768 ± 32 °C; 1s.d.) and reach markedly higher and similar temperatures at ages >1 Ma and <40 ka. Although ages are lacking for TB2 zircon at secular equilibrium, those that are <350 ka show a similar pattern in temperature evolution to those of TBJ, ranging between 810 °C and 703 °C, with an average of 759 ± 28 °C. In contrast, zircon crystals from TB3 and TB4 show significantly lower average crystallization temperatures of 722 ± 20 °C and 745 ± 20 °C, respectively. Low temperatures in TB3 and TB4 are particularly prevalent for ages <60 ka (Figure 6b). For comparison, zircon saturation temperatures (Boehnke et al., 2013) based on Zr abundances in glass are typically higher than the corresponding Ti-in-zircon temperatures except for TBJ.

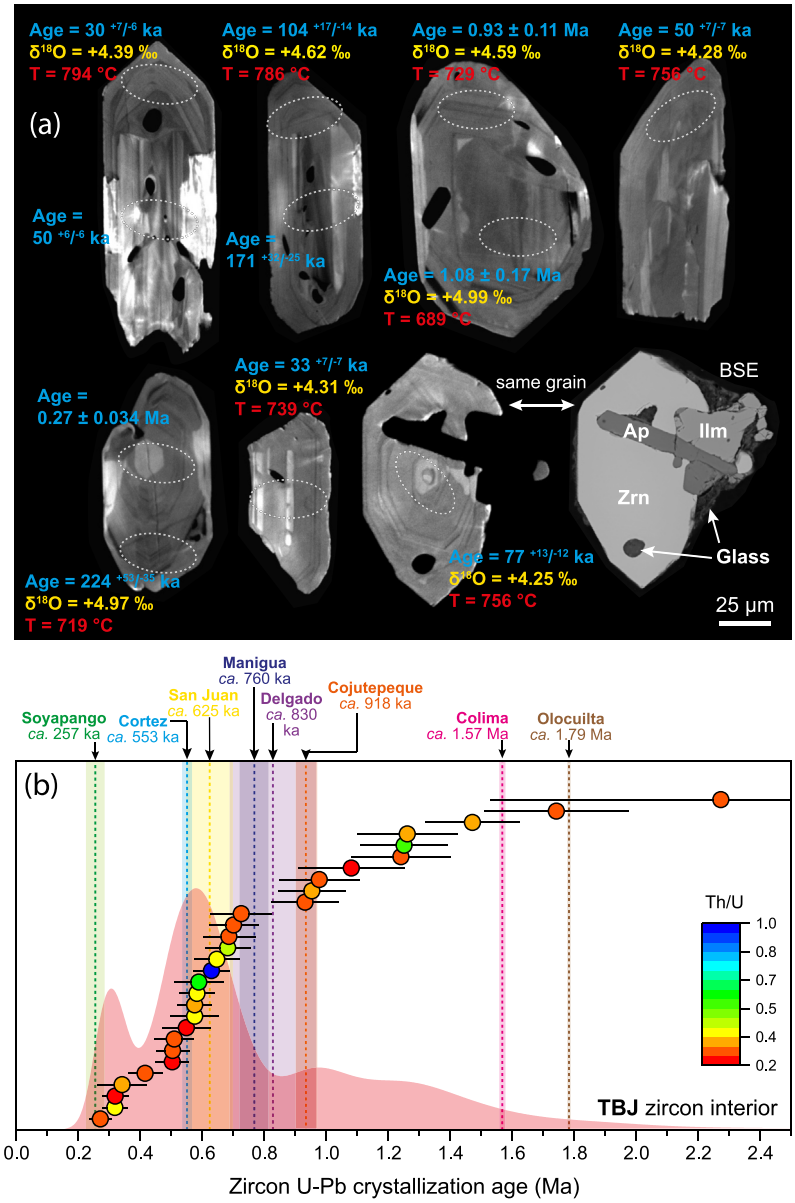

Figure 5. Crystal interior CL imaging and dating results for TBJ zircon. (a) CL and back-scattered electron (BSE) images of zircon interiors from TBJ eruption including age, oxygen isotopic composition, and Ti-in-zircon crystallization temperatures; (b) Ranked-order plot of disequilibrium-corrected U-Pb zircon crystallization ages. Color in symbols represent Th/U values. The underlying PDF was constructed from $^{238}U/^{206}Pb$ dates. Dashed lines are eruption ages for older units from Ilopango caldera (Suñe-Puchol et al., 2019a, 2019b).

4.7. Oxygen Isotopes in Zircon

TBJ zircon exhibit a narrow range of $\delta^{18}O$ values that are lower relative to mantle zircon (5.3 ± 0.3‰; Valley, 2003). These range from +3.94‰ to +5.08‰ with an average of +4.51 ± 0.24‰ (1 standard deviation; Figure S4). Miocene zircon xenocrysts show higher, mantle-like $\delta^{18}O$ values of +5.46‰ and +5.61‰. Multiple spots on TBJ single zircon crystals reveal homogeneous core and mantle domains within error although many crystals show intra-grain textural discontinuities (inset Figure S4). Time-integrated $\delta^{18}O$ compositions (Figure 7a) show, on average, slightly higher $\delta^{18}O$ values in zircon >100 ka (average = +4.62 ± 0.04‰; mean square weighted deviation MSWD = 0.91; n = 25), whereas zircon <100 ka tends toward lower $\delta^{18}O$ values (+4.40 ± 0.04‰; MSWD = 1.05; n = 29). Coeval zircon crystals yielded a $\delta^{18}O$ isotopic difference of <1‰. Although the difference between both age populations is only marginally resolved, it is emphasized

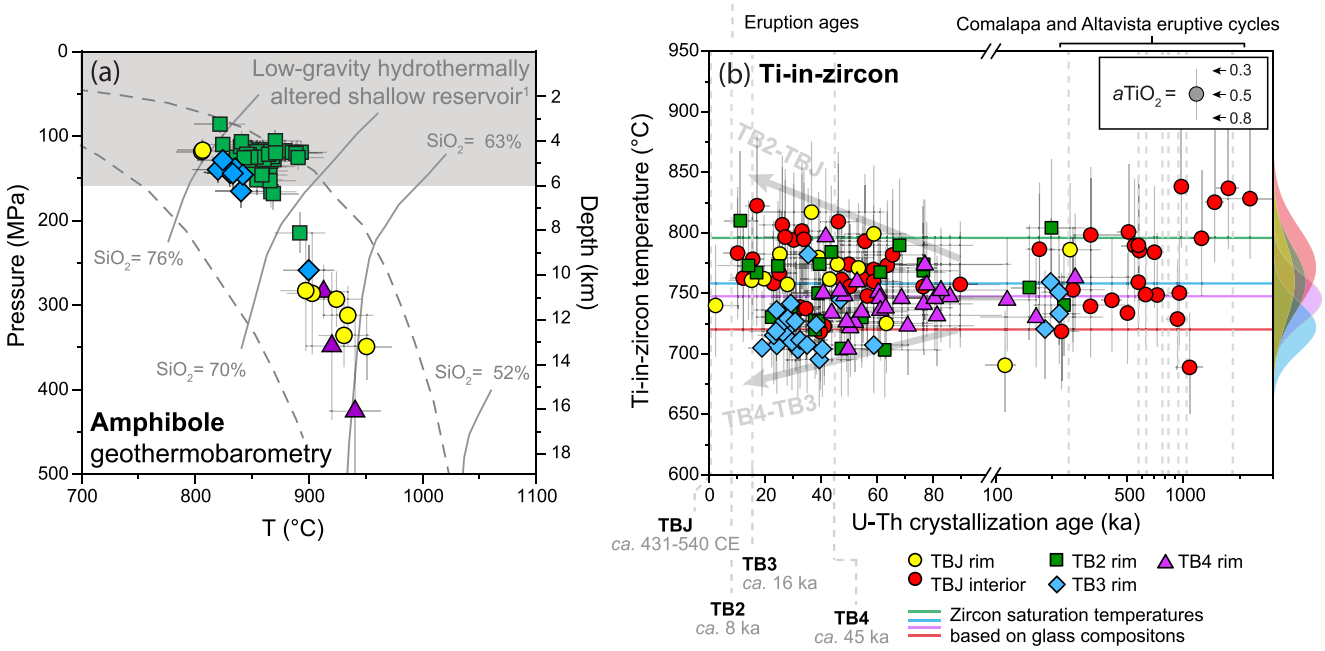

Figure 6. Mineral geothermobarometry for the TB suite. (a) Amphibole geothermobarometry based on Ridolfi et al. (2010). (b) Ti-in-zircon temperatures over time for the TB eruption suite. Vertical error bars represent uncertainties resulting from unknown titania activity values. Zircon saturation temperatures were calculated based on glass compositions and the calibration of Boehnke et al. (2013). PDFs for Ti-in-zircon temperatures are shown along the right-side *Y* axis with color-coding similar to the samples.

that all zircon crystals were analyzed on the same mount and in the same session, so a systematic instrumental bias is unlikely.

4.8. Trace Elements in Zircon

In general, TBJ and TB2 zircon are chemically similar and show a slightly more restricted range of Zr/Hf (38–53 and 40–56, respectively) than zircon in TB3 and TB4 (39–59 and 36–60, respectively; Table S4). There is a well-defined negative Eu/Eu* anomaly in zircon from all TB units, which is linked to the degree of previous feldspar fractionation (inset Figure S5). Differentiation indices reveal fluctuations during the ca. 2 Myr duration of zircon crystallization (Figure 7). Excursions to less evolved compositions correlate with known eruption cycles of Ilopango. For instance, zircon coeval to the Comalapa and Altavista eruptive cycles (>250 ka) show less evolved compositions (e.g., higher Zr/Hf) than zircon crystallizing within the repose periods (Figures 7b–7d). Similar chemical behavior is observed in zircon postdating the onset of the TB eruptive activity (<40 ka). Furthermore, in some cases, zircon coeval with major eruptive cycles display excursions to higher temperatures (Figures 7e–7h), and elemental abundances of U, Th, and Y commonly spike a few millennia prior to eruption (Figure sS6).

5. Discussion

5.1. Zircon ^{238}U-^{230}Th Crystallization Ages as Constraints for the Timing of Magma Accumulation and Eruption

The youngest zircon crystallization modes in the age spectra from TB4 to TB2 eruptions become progressively younger, consistent with stratigraphic superposition. In contrast, TBJ shows multiple crystallization peaks that correlate with those observed in older eruptions of the TB suite. Model eruption ages for TB2, TB3, and TB4 were calculated by applying a bootstrapped Bayesian approach to a truncated kernel density function constructed by the zircon ^{238}U-^{230}Th crystallization ages (Keller et al., 2018). The resulting eruption age estimates closely conform to the stratigraphic constraints and, in the case of TBJ, to the radiometrically determined age of ca. 431–545 CE that is currently the best estimate age range for this eruption (Table 1;

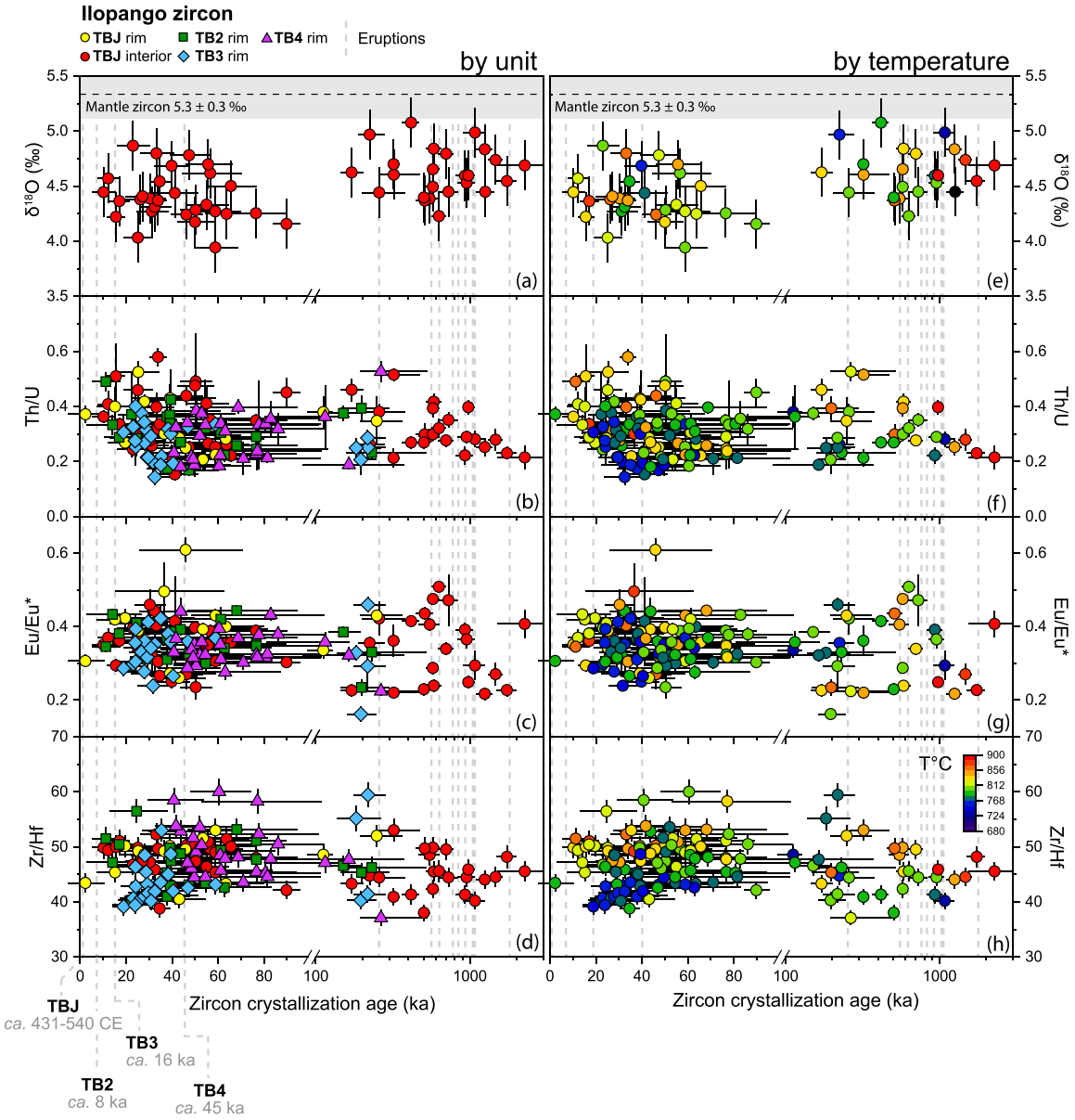

Figure 7. Oxygen isotopes and trace element compositions of zircon plotted against crystallization age. (a–d) Time-resolved zircon compositions and differentiation indices separated by eruptive units; (e–h) Zircon from the TB suite units taken as a single population with symbol colors representing Ti-in-zircon temperatures. Errors bars are 1σ. Dashed lines represent known radioisotopic eruption ages and eruption estimates from ^{238}U-^{230}Th zircon crystallization ages (e.g., TB2–TB4).

Dull et al., 2019; Smith et al., 2020). Similarly, the eruption age estimate for sample TB4 (45 ± 4.6 ka) is close to the ca. 36 ka estimated previously from sedimentation rates (Kutterolf et al., 2008). Hence, we consider the eruption age estimates of 8.3 ± 6.4 and 16 ± 7.8 ka for TB2 and TB3, respectively, as reasonable approximations for the ages of these presently undated eruptions. These eruption age estimates are hereafter applied to calculate the timescales of crustal magma residence (e.g., Brown & Fletcher, 1999; Costa, 2008; Reid & Coath, 2000; Reid et al., 1997; Schmitt et al., 2003; Vazquez & Reid, 2002), acknowledging that these are minima because of the possibility that the true eruption age is younger than the age inferred from ^{238}U-^{230}Th zircon crystallization ages.

The ca. 2 Myr eruptive and zircon record of Ilopango caldera (Lexa et al., 2011; Suñe-Puchol et al., 2019a) implies a long-lived (>10^5 yr) at least intermittently active transcrustal magmatic system (e.g., Cashman et al., 2017). This conforms with the protracted longevity of silicic magmatism invoked for many other

subvolcanic and plutonic settings (Bachmann & Bergantz, 2004; Gelman et al., 2013; Karakas et al., 2017). However, invoking a ca. 2 Myr continuous melt-dominated magma body below Ilopango caldera is unrealistic because of the following observations: (1) a protracted zircon age record (with ages >350 ka) is restricted to the youngest TBJ tephra; old zircon crystals are scarce in older eruptions based on the number of crystals in secular equilibrium for each sample (Figure 4); (2) TBJ zircon interiors commonly show intra-grain discontinuities which may suggest remobilization from subsolidus conditions or mushy domains (Figure 5); and (3) a hiatus in zircon crystallization between ca. 100 and 160 ka exists in all TB samples (including TBJ interiors), which overlaps a lull in eruptive activity between ca. 45 and 257 ka and suggests a magmatic system undergoing intermittent shutdown (Figure 4). Hence, heterogeneous zircon ages in TBJ likely reflect extensive zircon remobilization from solid or mushy portions of the reservoir during the build-up of the cataclysmic eruption instead of a prolonged (ca. 2 Myr) presence of a melt-rich subvolcanic magma chamber.

The true longevity of the last magmatic cycle at Ilopango is thus better represented by overlapping zircon ages younger than ca. 100 ka; these are present in all four TB eruptions. Extended timespans of quasi-continuous zircon crystallization of ca. 45 kyr (TB4), 42 kyr (TB3), 80 kyr (TB2), and 100 kyr (TBJ) are calculated from the difference between eruption age and the <100 ka semicontinuous zircon record. These are of the same magnitude as magma residence durations inferred for other silicic caldera systems (e.g., Charlier et al., 2005; Costa, 2008; Miller & Wooden, 2004; Reid & Coath, 2000; Vazquez & Reid, 2004). We use the term quasi-continuous zircon crystallization to acknowledge that ^{238}U-^{230}Th geochronology alone cannot distinguish between truly continuous crystallization and brief intermittent hiatuses that are below the dating resolution (e.g., Kent & Cooper, 2017). Age gaps between the major zircon crystallization peaks and corresponding eruption ages vary in a narrow range from ca. 12 kyr to ca. 15 kyr for TB2, TB3, and TB4 eruptions, whereas TBJ lacks a single prominent zircon crystallization maximum and ages predate the climactic eruption by several tens of thousands of years (Figure 8a). The apparent youngest zircon age mode of TBJ at ca. 15 ka (combining rim and interior data; Figure 8b) is either part of a recycled zircon component or an indication of renewed zircon crystallization in the magma chamber over a decamillennium and a half prior to eruption (ca. 431–545 CE). The nature of multiple peaks in zircon age spectra remains controversial, and explanations range from magma assembly from different magma batches to remobilization of solidified parts of the magma reservoir where zircon crystallized at different times (Bacon & Lowenstern, 2005; Charlier et al., 2005; Miller & Wooden, 2004; Reid & Vazquez, 2017; Schmitt et al., 2003, 2010; Storm et al., 2011). Multiple zircon crystallization peaks could also be an artifact of the low number of analyses (<30 analyses; Frey et al., 2018), and confident identification of distinct zircon growth episodes would require the identification of age gaps, either from truncation of internal growth zones due to intermittent resorption or from sharp age increments in depth profiling analyses (Frey et al., 2018; Reid & Vazquez, 2017; Storm et al., 2012). Although the total number of crystals analyzed for individual TBJ units in this study was 38 and 72 for rim and core ages, respectively, the number of analyses in the <100 ka range is smaller, and therefore apparent modes within the <100 ka interval may lack statistical significance. By contrast, when combining TB2, TB3, and TB4 zircon age populations into one, the resulting PDF shows a strong similarity to the combined TBJ rim and interior zircon population that is also confirmed by similarity statistical tests (Kolmogorov-Smirnov statistics based on slope values with symmetrical errors; Figure 8; e.g., Schmitt et al., 2010). This includes zircon crystallization age peaks in TBJ (e.g., ca. 55 and 30 ka) that match those observed in the constructed PDF with older eruptions (e.g., TB2–TB4; Figure 8b). This supports a scenario where quasi-continuous zircon crystallization occurred in the last ca. 100 kyr in different storage zones of the magma reservoir, which individually may have been more short-lived than the entire subcaldera magma system. Nonetheless, zircon antecrysts of different origins became mixed or juxtaposed at a later point and co-erupted, with the most heterogeneous age population in the youngest and largest TBJ eruption. This likely happened during a post-8 ka (based on the estimated eruption age of TB2) rejuvenation and growth event of the Ilopango eruptible magma chamber that may not have been unique, but of higher intensity than previous events.

5.2. Evidence for Melt Interaction Between Deeper and Shallower Parts in a Transcrustal Magmatic Reservoir

A paucity of zircon crystallization between ca. 100 and 160 ka is observed in all TB eruptions and may provide corroborating evidence for discontinuous magma presence within the reservoir due to transient subsolidus conditions. Alternatively, a minimum in zircon crystallization ages could also reflect the presence of

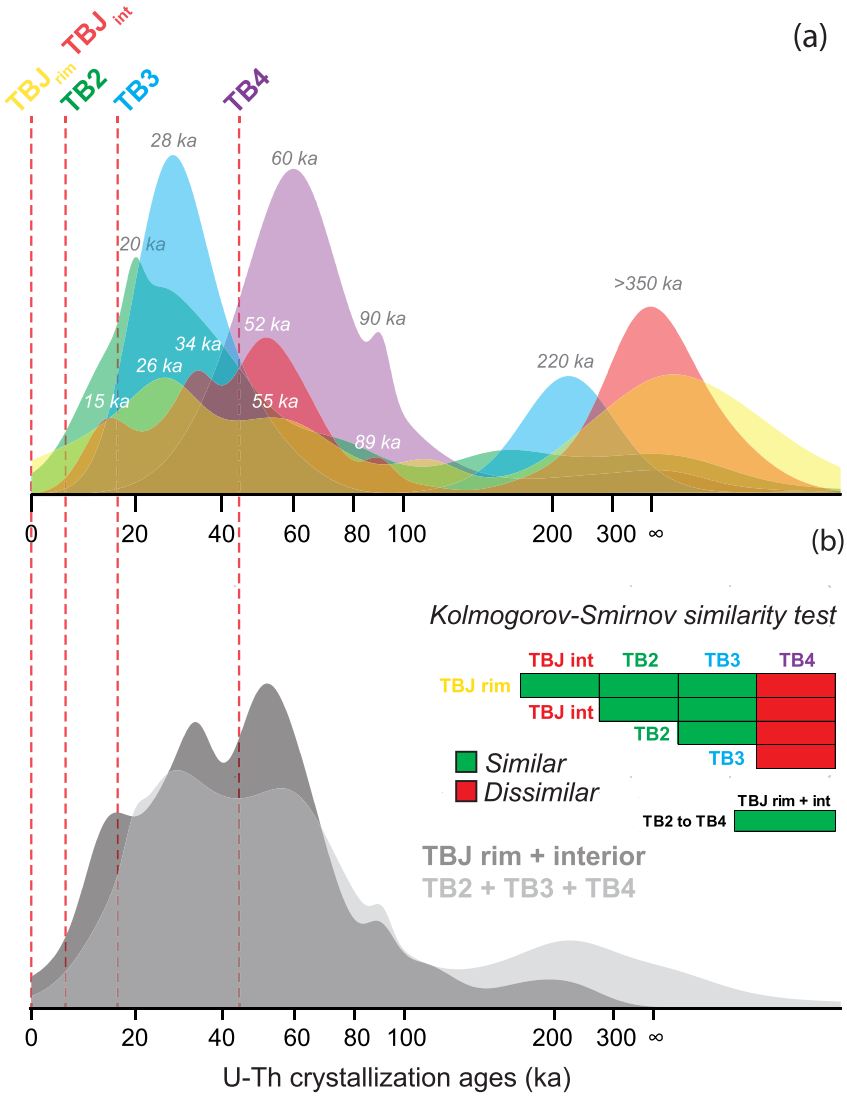

Figure 8. Zircon age distribution comparisons. (a) Comparison of all individual zircon rim age PDF curves including TBJ zircon interiors; (b) PDF curves constructed from merging zircon age data from TBJ rims and interiors (dark gray) and TB2, TB3, and TB4 rims (light gray). Inset shows probabilities for zircon populations being identical (green) versus distinct (red) based on Kolmogorov-Smirnov statistical analysis; dashed red lines represent eruption age (TBJ) and eruption age estimates (TB2, TB3, and TB4).

zircon undersaturated magmas where zircon failed to nucleate or became subsequently resorbed. Because all TB eruptions contain zircon with ages predating the zircon crystallization age gap (ca. 160 to >350 ka), selective resorption of zircon that crystallized between ca. 100 and 160 ka is an unlikely scenario. Also, if zircon undersaturated, more mafic magma dominated the subvolcanic reservoir between ca. 100 and 160 ka, it is difficult to explain why it did not erupt despite its lower crystallinity compared to the evolved magmas of the subsequently erupted TB suite. Thus, the zircon crystallization gap is preferentially explained by an intermittent thermal shutdown where the volcanic plumbing system of Ilopango caldera transiently reached subsolidus conditions following the ca. 257 ka Soyapango eruption. This would allow preservation of preexisting zircon in "cold storage," which also survived subsequent remobilization when eruptive activity resumed with TB4.

Magmas tapped during the TB eruptions contain crystalline materials derived from thermally and compositionally distinct storage zones of the magmatic reservoir which most likely coexisted at different depths during the post-60 ka evolution of the system. This is based on (1) significant chemical and thermal differences

in contemporaneous zircon present in TB eruption products (Figure 7) and (2) contrasting amphibole crystallization temperatures and pressures among TB eruptions (Figure 6a). Variable contributions of deeper and shallower silicic magmas are notably reflected by the contrasting temperatures recorded by contemporaneous zircon among distinct TB eruptions (Figure 6b) as well from different ranges of pressure and temperature obtained from major minerals such as amphibole (Figure 6a). Overall, thermochemical indicators in zircon for all TB eruptions tend to converge at low-T, highly fractionated conditions at ~700 °C and with low Zr/Hf (Figure 7d), but there are distinct fields for high-T and less fractionated zircon (high Zr/Hf) for TB2 and TBJ relative to low-T and more fractionated zircon (low Zr/Hf) for TB4 and TB3. Although TB4 and TB3 zircon populations are statistically different based on Ti-in-zircon temperatures (according to a non-parametric statistical *U* test; Mann & Whitney, 1947), they define a continuous trend in temperature versus Zr/Hf (Figure S5). This contrasts with higher temperatures at comparatively low Zr/Hf in <40 ka TB2 and TBJ zircon. The observed diverging evolution in Ti-in-zircon thermometry among TB eruptions hints at different $a\mathrm{TiO_2}$ in individual coexisting storage zones of the magma reservoir.

Although amphibole thermobarometry has considerable uncertainties (Ridolfi et al., 2010), the pressure results from TB2 and TB3 (Figure 6a) match the shallow reservoir depths of up to ~6 km detected by geophysical investigations (Saxby et al., 2016). Other amphibole crystals, mainly present in TBJ and TB4, yielded pressure estimates that correspond to at least ≥9 km depth. Temperature estimates also slightly differ, with 800–900 °C for the shallow amphibole, and >900 °C for deep amphibole crystallization. Contemporary zircon from TBJ and TB2 exhibit a similar bimodality in temperature as the amphibole, and although temperatures of >900 °C suggested by amphibole would imply zircon undersaturated conditions, these elevated temperatures might be transient due to magma recharge from even greater depths, and therefore some zircon from the lower portions of the reservoir would have been transported upward into the shallower magma assembly.

Regarding the timescales of interaction between melts of different storage zones within the reservoir and the ultimate assembly of eruptible magma at shallow levels, we take the youngest preeruptive zircon crystallization age peak as an indication for the last magma cooling episode prior to an eruption. This assumes that zircon preferentially crystallized during cooling, whereas magma buildup prior to an eruption is associated with recharge causing heating and thus limiting zircon crystallization as evident from the frequent partial dissolution of zircon surfaces in TBJ and the low number of zircon rims overlapping the eruption date. The minimum longevity of the magma chamber at eruptible conditions could be inferred as the period between the last magma cooling event (which caused a pulse in zircon growth) and the eruption age. This timespan is similar for all eruptions including the voluminous TBJ (between ca. 12 and 15 kyr) and are at the lower limit of the 10^4–10^6 yr intervals previously proposed for differentiation and segregation of evolved melts (Bachmann & Bergantz, 2004; Fowler & Spera, 2010; Reid et al., 1997; Rivera et al., 2016; Spera, 1980; Wotzlaw et al., 2014). They are also compatible with brief durations (<10 kyr) of major phase crystallization as indicated by ^{238}U-^{230}Th mineral isochrons from TBJ (Garrison et al., 2012) and support comparatively rapid aggregation of magma that ultimately erupted as the TBJ cataclysm (Figure 3d).

5.3. Contrasting Crystallization Timescales for Zircon and Major Minerals

Zircon crystallization ages significantly predate the onset of preeruptive crystallization of pyroxene, amphibole, magnetite, and plagioclase which are <10 ka based on previously reported major mineral ^{238}U-^{230}Th isochrons for the TBJ from Garrison et al. (2012). This age offset between accessory zircon and the major minerals in TBJ is intriguing and consistent with the petrographic observation that zircon frequently occurs as inclusions in the major phases. For different TB eruptions, the contributions of juvenile versus recycled from crystal mushes crystals vary significantly. For instance, although showing partial age overlap, TB4 and TB3 zircon age populations are statistically distinct (inset Figure 8), with few TB4-aged zircon in TB3 magma, yet they define a coherent thermochemical trend over time (Figure 6). The colder (~700 °C) and highly evolved nature (low Zr/Hf) of zircon in TB3 magma suggest crystallization within a crystal-rich magma reservoir that underwent cooling after the voluminous TB4 magma evacuation (~36 km^3). Numerous glomerocrystic inclusions in TB3 pumice are tentatively interpreted as relics for such crystal-rich mushes (Figure S2). Although coeval crystallization between zircon and amphibole cannot be a priori assumed, TB3 amphibole nevertheless supports preeruptive magma residence in a shallow and comparatively colder

(~800 °C) reservoir. Potential evidence of magmatic consanguinity between TB4 and TB3 magmas comes from similar major (with exception of CaO wt.%) and trace element compositions of matrix glasses, whereas TBJ and TB2 glass compositions are distinct (Figure 2 and Figure S3).

The evolution of TB2 magma likely started with the emplacement of a relatively less evolved dacitic and hot magma (>750 °C) into the shallow reservoir. This is indicated by Sr-Nd isotope compositions of TB2 magma shifting toward less radiogenic compositions compared to TB3 (Figures 3b and 3c). Assembly and residence of TB2 melt within a shallow magma chamber was likely short (<8 kyr; the difference between TB3 and TB2 eruption ages), and the overlapping thermal and chemical zircon histories between TB2 and TBJ further suggest that the comparatively small TB2 eruption (1–5 km^2) may have only tapped a small "mobile" fraction of the much larger reservoir that eventually fed the TBJ eruption (e.g., Mahood, 1990). The presence of TB3-like zircon in TB2 and TBJ magmas can be explained by the remobilization of the crystallized portions of the magma reservoir prior to eruption. Thus, TB2 eruption most likely marks the onset of a significant spatial re-organization of the magma chamber in response to increasing recharge from deeper dacite into the upper part of the magma reservoir leading to a renewed excursion toward higher temperatures in the shallow crust as a result of crust thermal maturation (e.g., Karakas et al., 2017).

The TBJ eruption, which is the youngest and most voluminous of the suite, contains zircon with a complex, polymodal age distribution with overlapping modes for rim and interior domains, especially for zircon ages <100 ka. The polymodal age distribution in TBJ is likely associated with extensive remobilization of and zircon recycling from older crystal mushes or solidified portions of the upper magma reservoir (Figure 9). The absence of such zircon age complexity in older TB eruptions place constraints on the timing of crystal remobilization as TB2 magma that erupted at ca. 8 ka lacks a similar zircon age complexity. The extensive remobilization process was likely a consequence of higher recharge rates of comparatively unevolved and zircon-undersaturated magmas during the last ca. 8 kyr, which is reflected by the negligible crystallization of zircon during this time interval. A prograde thermal evolution due to rejuvenation by the input of hotter, less differentiated magmas shortly before eruption is consistent with the preservation of disequilibrium textures like corrosion of TBJ zircon surfaces (Figure 4a). Zircon saturation temperatures for TBJ glass (~717 °C; Boehnke et al., 2013; Watson & Harrison, 1983) which are lower than zircon and amphibole thermometry suggest that equilibrium between zircon and melt has not been fully reached in the time since magma recharge.

Relatively rapid assemble of the TBJ magma chamber is also supported by bulk crystal ^{238}U-^{230}Th analysis of amphibole (Garrison et al., 2012), which indicates crystallization ages that are close to the 0 ka reference line (Figure 3c). Acknowledging that bulk crystal analysis may average crystals of different ages, this zero-age for amphibole indicates that the majority of amphibole phenocrysts are of very recent age. Diffusive reequilibration of Th and U in amphibole can also be ruled out based on slow diffusivities of tetravalent cations (Cherniak & Dimanov, 2010), whereas rapid (within <<10 kyr) crystallization of amphibole is consistent with experimentally calibrated growth rates (Zhang et al., 2019). The complete lack of antecrystic amphibole, and likely of other major phases that also crystallized shortly before eruption (Garrison et al., 2012), is in stark contrast to zircon, where only two rim analyses are within error of the eruption age. Paradoxically, zircon only reaches saturation in melts with the TBJ glass composition at comparatively low temperatures (~717 °C), and the Ti-in-zircon thermometry for antecrystic zircon indicates significantly lower crystallization temperatures. Under such conditions, a high abundance of crystals should have formed, but these do not contribute to the crystal inventory of TBJ. We, therefore, propose that zircon immersed in the rhyolitic melt, was segregated from viscous crystal-rich domains of the magma reservoir of likely dacitic bulk composition after compaction, driven by the loading exerted by the crystal mush itself (e.g., Holness et al., 2018; McKenzie, 2011) or from gas filter-pressing melt extraction processes (Hartung et al., 2017). The extracted interstitial melt then mixed and homogenized rapidly with newly emplaced, initially crystal-poor magma that then started to crystallize ≥9 km deep and subsequently migrated upward into a shallow reservoir at ≤6 km, as indicated by the compositionally heterogeneous amphibole (Figure 6a).

5.4. Multicomponent Assimilation in TB Magma Genesis

The unusual positive Sr-Nd isotopic array of TBJ and other CAVA rocks (Figures 3a and 3b; compare the negative slope of the mantle array: MORB and OIB) has been explained by magma mixing between basaltic

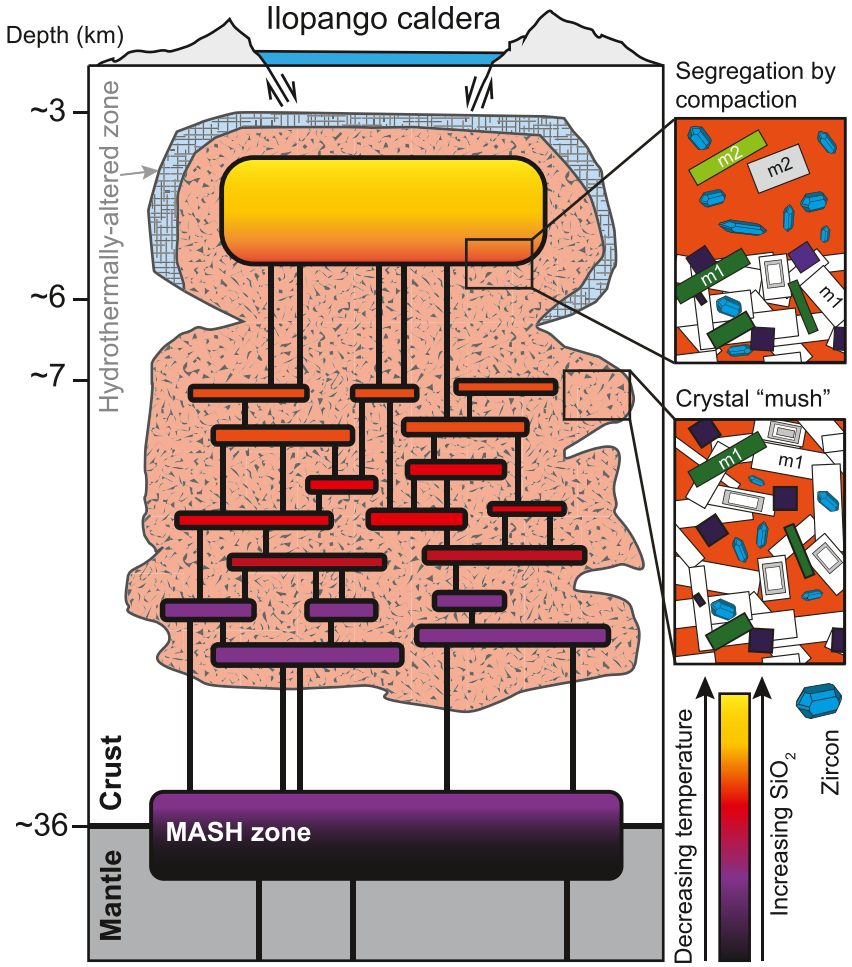

Figure 9. Conceptual model (dimensions not to scale) of the transcrustal magma system below Ilopango caldera. The proposed magmatic system is volumetrically dominated by long-lived and largely immobile "crystal mush" (>50% crystals) with segregations of sill-like melt-rich bodies (e.g., Cashman et al., 2017). Magma bodies within the system become progressively SiO_2-enriched upsection due to cooling, crystallization, and assimilation of wall rock. Zircon saturated silicic magma bodies within the upper crust are envisioned to have formed after extraction and segregation of interstitial melt from different parts of the crystal mush due to compaction or reactive flow processes (e.g., Holness et al., 2018). During TBJ magma chamber assembly, the rhyolitic-dacitic melt was transferred upward into a shallow magma chamber, leaving behind an older major mineral crystal residue (m1), whereas zircon of equivalent age was extracted suspended in the melt. Before eruption (<10 kyr), a newer generation of major minerals crystallized in the shallow magma chamber (m2). Moho depth from Lücke et al. (2014).

andesite (represented by enclaves) and melts derived from the sedimentary Chortis Block basement (Garrison et al., 2012), or from melting in the mantle wedge in response to fluids derived from the sedimentary slab-component (enriched in $^{87}Sr/^{86}Sr$ by sea water; Carr, Feigenson, & Bennett, 1990; Feigenson & Carr, 1986). However, both models fail to explain the observed low-$\delta^{18}O$ isotopic compositions in Ilopango zircon (Figure S4), as sediments would increase the bulk $\delta^{18}O$ signature of the source (typical are of +20–30‰; Eiler, 2001). Models for crystallization of zircon with low-$\delta^{18}O$ (relative to mantle values of +5.3 ± 0.3‰) invoke assimilation of hydrothermally altered crustal rocks that interacted with low-$\delta^{18}O$ meteoric water at high temperatures (e.g., Yellowstone zircon; Bindeman, 2008; Eiler et al., 2005; Valley, 2003). Whether these components are derived from remelting of contemporaneous hydrothermally altered downdropped blocks (Bindeman et al., 2001; Bindeman & Valley, 2001; Cheong et al., 2017) or the preexisting hydrothermally altered basement is difficult to recognize (Boroughs et al., 2005).

Zircon from TBJ spanning ca. 2 Myr consistently shows low-$\delta^{18}O$ values (average +4.51‰ ± 0.24; $n = 55$; Figure 7a) relative to the mantle. These signatures cannot be produced by fractionation between silicate

melts and minerals (Valley, 2003), nor by postcrystallization modification of oxygen isotopes in zircon by diffusion at near-magmatic temperatures (Bindeman et al., 2018; Cisneros de León & Schmitt, 2019). Moreover, Miocene zircon xenocrysts within TBJ tephra ($n = 2$) yielded mantle-like compositions (~+5.5‰) that differ significantly from TBJ zircon. If these xenocrysts were derived from subducted sediment or pristine silicic crustal basement, then the low-$\delta^{18}O$ signatures in TBJ zircon are also unlikely to be derived from the source or via lower crustal assimilation. Although the number of identified zircon xenocrysts is small, "normal" $\delta^{18}O$ in TB parental magmas is further supported by mantle-like or higher $\delta^{18}O$ values of olivine (+5.1–5.6‰; Eiler et al., 2005) from Quaternary basaltic to andesitic volcanoes which erupted adjacent to Ilopango caldera (e.g., Cerro Verde, Izalco, and Apastepeque). However, assimilation of hydrothermally altered intracaldera components can explain the decrease in $\delta^{18}O$ compositions of Ilopango zircon. Antecrystic cores and juvenile overgrowths show remarkably similar low-$\delta^{18}O$ compositions, and their age difference is generally <100 kyr, implying that any assimilated zircon already had low-$\delta^{18}O$ values. This suggests that the low-$\delta^{18}O$ zircon signature resulted from long-lived recycling of juvenile hydrothermal components. We envision a two-stage model where either source contamination or fore arc assimilation initially shifted the Sr-Nd-O-isotope compositions of primitive magma to higher values (e.g., Cameron & Walker, 2006), and subsequent assimilation of a genetically related hydrothermally altered carapace. Although subtle (<1‰) but statistically discernable, zircon crystallized from >100 ka magmas exhibit on average higher $\delta^{18}O$ values than those observed in zircon <100 ka (Figure 7). This may suggest that assimilation of hydrothermally altered intracaldera rocks became more extensive toward the end of the most recent TB eruptive cycle (e.g., Bindeman et al., 2008).

6. Conclusion

Zircon petrochronology at high-spatial-resolution provides insights into the evolution and processes of magmas residing in the upper crust otherwise difficult to retrieve from bulk-samples erupted intermittently over time. Eruption age estimates for radioisotopically undated Ilopango caldera eruptions are ca. 8.3 ± 6.4 ka (TB2), 16 ± 7.8 ka (TB3), and 45 ± 4.6 ka (TB4) based on a population-based Bayesian model for preeruptive zircon crystallization. Collectively, zircon from Ilopango caldera shows a record encompassing a protracted production of silicic magmas over the last ca. 2 Myr, whereby the last four eruptions (TBJ, TB2, TB3, and TB4) gestated from silicic magmas residing in the upper crust during the last ca. 100 ka. Individual preeruption storage timescales are >40 kyr prior to eruption according to the zircon data. This is in contrast to the short timescales (<10 kyr) obtained from major mineral phases. Such residence time dichotomy is explained by crystal-melt segregation in which a rejuvenated and eruptible magma body (bearing older zircon) is formed and from which major mineral phases crystallized briefly before the eruption. The geochemistry and crystallization temperatures of zircon for individual eruptions indicate divergent thermal and chemical evolution between TB4-TB3 eruptions on the one hand and TB2-TBJ eruptions on the other, suggesting coeval storage and supply of silicic magma from different crustal levels. Low-$\delta^{18}O$ (average = +4.5‰) signatures in zircon since ca. 2 Ma indicate continuous recycling of shallow hydrothermally altered components from within Ilopango caldera.

Conflict of Interest

The authors declare no conflict of interest relevant to this study.

Data Availability Statement

Geochronological and geochemical data produced during this study can be found at Cisneros de León et al., 2021 in PANGAEA Data Archiving and Publication (https://doi.org/10.1594/PANGAEA.929673). An electronic copy of this data file is provided as Tables S1–S9. The authors have no conflict of interest to declare.

Acknowledgments
This study was financially supported by the Deutsche Forschungsgemeinschaft (Projects DFG SCHM 2521/6-1 and DFG KU2685/7-1). We thank Thomas Ludwig and Alexander Varychev for support during the SIMS oxygen isotope analyses and SEM imaging. Ilona Fin and Oliver Wienand are thanked for sample preparation. Holli Frey, Jorge Vázquez, an anonymous reviewer, and Editor Marie Edmonds are thanked for their constructive criticism that helped to improve this manuscript. Finally, we are very grateful to the Environmental Observatory of the Ministry of Environment and Natural Resources of El Salvador (MARN), for providing us with logistical support during fieldwork.

References

Annen, C., Blundy, J. D., & Sparks, R. S. J. (2006). The genesis of intermediate and silicic magmas in deep crustal hot zones. *Journal of Petrology*, *47*, 505–539. https://doi.org/10.1093/petrology/egi084

Annen, C., & Sparks, R. S. J. (2002). Effects of repetitive emplacement of basaltic intrusions on thermal evolution and melt generation in the crust. *Earth and Planetary Science Letters*, *203*, 937–955. https://doi.org/10.1016/s0012-821x(02)00929-9

Bachmann, O., & Bergantz, G. W. (2004). On the origin of crystal-poor rhyolites: Extracted from batholithic crystal mushes. *Journal of Petrology*, *45*, 1565–1582. https://doi.org/10.1093/petrology/egh019

Bacon, C., & Lowenstern, J. (2005). Late Pleistocene granodiorite source for recycled zircon and phenocrysts in rhyodacite lava at Crater Lake, Oregon. *Earth and Planetary Science Letters*, *233*, 277–293. https://doi.org/10.1016/j.epsl.2005.02.012

Bégué, F., Deering, C. D., Gravley, D. M., Kennedy, B. M., Chambefort, I., Gualda, G. A., & Bachmann, O. (2014). Extraction, storage and eruption of multiple isolated magma batches in the paired Mamaku and Ohakuri eruption, Taupo Volcanic Zone, New Zealand. *Journal of Petrology*, *55*(8), 1653–1684.

Bergantz, G. W., Schleicher, J. M., & Burgisser, A. (2015). Open-system dynamics and mixing in magma mushes. *Nature Geoscience*, *8*, 793–796. https://doi.org/10.1038/ngeo2534

Bindeman, I. (2008). Oxygen isotopes in mantle and crustal magmas as revealed by single crystal analysis. *Reviews in Mineralogy and Geochemistry*, *69*, 445–478. https://doi.org/10.2138/rmg.2008.69.12

Bindeman, I., Schmitt, A., Lundstrom, C., & Hervig, R. (2018). Stability of zircon and its isotopic ratios in high-temperature fluids: Long-term (4 months) isotope exchange experiment at 850° C and 50 MPa. *Frontiers of Earth Science*, *6*, 59. https://doi.org/10.3389/feart.2018.00059

Bindeman, I. N., Fu, B., Kita, N. T., & Valley, J. W. (2008). Origin and evolution of silicic magmatism at Yellowstone based on ion microprobe analysis of isotopically zoned zircons. *Journal of Petrology*, *49*, 163–193. https://doi.org/10.1093/petrology/egm075

Bindeman, I. N., & Valley, J. W. (2001). Low-δ^{18}O rhyolites from yellowstone: Magmatic evolution based on analyses of zircons and individual phenocrysts. *Journal of Petrology*, *42*, 1491–1517. https://doi.org/10.1093/petrology/42.8.1491

Bindeman, I. N., Valley, J. W., Wooden, J. L., & Persing, H. M. (2001). Post-caldera volcanism: In situ measurement of U-Pb age and oxygen isotope ratio in Pleistocene zircons from Yellowstone caldera. *Earth and Planetary Science Letters*, *189*, 197–206. https://doi.org/10.1016/s0012-821x(01)00358-2

Boehnke, P., Watson, E. B., Trail, D., Harrison, T. M., & Schmitt, A. K. (2013). Zircon saturation re-revisited. *Chemical Geology*, *351*, 324–334. https://doi.org/10.1016/j.chemgeo.2013.05.028

Boroughs, S., Wolff, J., Bonnichsen, B., Godchaux, M., & Larson, P. (2005). Large-volume, low-δ^{18}O rhyolites of the central Snake River Plain, Idaho, USA. *Geology*, *33*, 821–824. https://doi.org/10.1130/g21723.1

Brenna, H., Kutterolf, S., Mills, M. J., & Krüger, K. (2020). The potential impacts of a sulfur- and halogen-rich supereruption such as Los Chocoyos on the atmosphere and climate. *Atmospheric Chemistry and Physics*, *20*, 6521–6539. https://doi.org/10.5194/acp-20-6521-2020

Brenna, H., Kutterolf, S., Mills, M. J., Niemeier, U., Timmreck, C., & Krüger, K. (2021). Decadal disruption of the QBO by tropical volcanic supereruptions. *Geophysical Research Letters*, *48*, e2020GL089687. https://doi.org/10.1029/2020GL089687

Brown, S. J. A., & Fletcher, I. R. (1999). SHRIMP U-Pb dating of the preeruption growth history of zircons from the 340 ka Whakamaru Ignimbrite, New Zealand: Evidence for >250 k.y. magma residence times. *Geology*, *27*, 1035–1038. https://doi.org/10.1130/0091-7613(1999)027<1035:SUPDOT>2.3.CO;2

Cameron, B., & Walker, J. (2006). Diverse volcanism in southeastern Guatemala: The role of crustal contamination. *Special Papers—Geological Society of America*, *412*, 121.

Carr, M. J. (1984). Symmetrical and segmented variation of physical and geochemical characteristics of the Central American volcanic front. *Journal of Volcanology and Geothermal Research*, *20*, 231–252. https://doi.org/10.1016/0377-0273(84)90041-6

Carr, M. J. (2017). A google earth database of central American volcanic vents. *Revista Geologica de America Central*, *56*, 7–15.

Carr, M. J., Feigenson, M. D., & Bennett, E. A. (1990). Incompatible element and isotopic evidence for tectonic control of source mixing and melt extraction along the Central American arc. *Contributions to Mineralogy and Petrology*, *105*, 369–380. https://doi.org/10.1007/BF00286825

Carr, M. J., Feigenson, M. D., Patino, L. C., & Walker, J. A. (2003). Volcanism and geochemistry in Central America: Progress and problems. In J. Eiler (Eds.), *Inside the Subduction Factory* (Vol. 138, pp. 153–174). Washington, DC: American Geophysical Union. https://doi.org/10.1029/138GM09

Cashman, K. V., & Giordano, G. (2014). Calderas and magma reservoirs. *Journal of Volcanology and Geothermal Research*, *288*, 28–45. https://doi.org/10.1016/j.jvolgeores.2014.09.007

Cashman, K. V., Sparks, R. S. J., & Blundy, J. D. (2017). Vertically extensive and unstable magmatic systems: A unified view of igneous processes. *Science*, *355*(6331), eaag3055.

Charlier, B. L. A., Wilson, C. J. N., Lowenstern, J. B., Blake, S., Van Calsteren, P. W., & Davidson, J. P. (2005). Magma generation at a large, hyperactive silicic volcano (Taupo, New Zealand) revealed by U-Th and U-Pb systematics in zircons. *Journal of Petrology*, *46*, 3–32. https://doi.org/10.1093/petrology/egh060

Cheong, A. C.-S., Sohn, Y. K., Jeong, Y.-J., Jo, H. J., Park, K.-H., Lee, Y. S., & Li, X.-H. (2017). Latest Pleistocene crustal cannibalization at Baekdusan (Changbaishan) as traced by oxygen isotopes of zircon from the Millennium eruption. *Lithos*, *284–285*, 132–137. https://doi.org/10.1016/j.lithos.2017.04.012

Cherniak, D. J., & Dimanov, A. (2010). Diffusion in pyroxene, mica and amphibole. *Reviews in Mineralogy and Geochemistry*, *72*, 641–690. https://doi.org/10.2138/rmg.2010.72.14

Cisneros de León, A., & Schmitt, A. K. (2019). Reconciling Li and O diffusion in zircon with protracted magmatic crystal residence. *Contributions to Mineralogy and Petrology*, *174*, 28. https://doi.org/10.1007/s00410-019-1564-8

Cisneros de León, A., Schmitt, A. K., Kutterolf, S., Schindlbeck-Belo, J., Hernández, W., Sims, K. W. W., et al. (2021). *Zircon petrochronology and tephra compositions of the last four explosive eruptions from Ilopango caldera (El Salvador)*. PANGAEA. https://doi.org/10.1594/PANGAEA.929673

Claiborne, L. L., Miller, C. F., Flanagan, D. M., Clynne, M. A., & Wooden, J. L. (2010). Zircon reveals protracted magma storage and recycling beneath Mount St. Helens. *Geology*, *38*, 1011–1014. https://doi.org/10.1130/g31285.1

Coffey, K. T., Schmitt, A. K., Ford, A., Spera, F. J., Christensen, C., & Garrison, J. (2014). Volcanic ash provenance from zircon dust with an application to Maya pottery. *Geology*, *42*, 595–598. https://doi.org/10.1130/g35376.1

Corti, G., Carminati, E., Mazzarini, F., & Garcia, M. O. (2005). Active strike-slip faulting in El Salvador, Central America. *Geology*, *33*, 989–992. https://doi.org/10.1130/g21992.1

Costa, F. (2008). Chapter 1: Residence times of silicic magmas associated with calderas. *Developments in volcanology*, *10*, 1–55. https://doi.org/10.1016/s1871-644x(07)00001-0

Dull, R. A., Southon, J. R., Kutterolf, S., Anchukaitis, K. J., Freundt, A., Wahl, D. B., et al. (2019). Radiocarbon and geologic evidence reveal Ilopango volcano as source of the colossal 'mystery' eruption of 539/40 CE. *Quaternary Science Reviews*, *222*, 105855. https://doi.org/10.1016/j.quascirev.2019.07.037

Dull, R. A., Southon, J. R., & Sheets, P. (2001). Volcanism, ecology and culture: A reassessment of the Volcán Ilopango TBJ eruption in the Southern Maya Realm. *Latin American Antiquity*, *12*, 25–44. https://doi.org/10.2307/971755

Eiler, J. M. (2001). Oxygen isotope variations of basaltic lavas and upper mantle rocks. *Reviews in Mineralogy and Geochemistry*, *43*, 319–364. https://doi.org/10.2138/gsrmg.43.1.319

Eiler, J. M., Carr, M. J., Reagan, M., & Stolper, E. (2005). Oxygen isotope constraints on the sources of Central American arc lavas. *Geochemistry, Geophysics, Geosystems*, *6*, Q07007. https://doi.org/10.1029/2004GC000804

Ellis, B. S., Szymanowski, D., Wotzlaw, J. F., Schmitt, A. K., Bindeman, I. N., Troch, J., et al. (2017). Post-caldera volcanism at the Heise volcanic field: Implications for petrogenetic models. *Journal of Petrology*, *58*, 115–136. https://doi.org/10.1093/petrology/egx007

Feigenson, M. D., & Carr, M. J. (1986). Positively correlated Nd and Sr isotope ratios of lavas from the Central American volcanic front. *Geology*, *14*, 79–82. https://doi.org/10.1130/0091-7613(1986)14<79:PCNASI>2.0.CO;2

Ferry, J. M., & Watson, E. B. (2007). New thermodynamic models and revised calibrations for the Ti-in-zircon and Zr-in-rutile thermometers. *Contributions to Mineralogy and Petrology*, *154*(4), 429–437.

Fowler, S. J., & Spera, F. J. (2010). A metamodel for crustal magmatism: Phase equilibria of giant ignimbrites. *Journal of Petrology*, *51*, 1783–1830. https://doi.org/10.1093/petrology/egq039

Frey, H. M., Manon, M. R. F., Brehm, S. K., & Babiak, R. N. (2018). Episodic crystallization in young explosive eruptions in Dominica, Lesser Antilles, revealed by U-Th dating of zircons. *Geology*, *46*, 887–890. https://doi.org/10.1130/g45217.1

Garrison, J. M., Reagan, M. K., & Sims, K. W. (2012). Dacite formation at Ilopango Caldera, El Salvador: U-series disequilibrium and implications for petrogenetic processes and magma storage time. *Geochemistry, Geophysics, Geosystems*, *13*, Q06018. https://doi.org/10.1029/2012GC004107

Gelman, S. E., Gutiérrez, F. J., & Bachmann, O. (2013). On the longevity of large upper crustal silicic magma reservoirs. *Geology*, *41*, 759–762. https://doi.org/10.1130/g34241.1

Hart, W. J. & Steen-McIntyre, V. (1983). Tierra Blanca Joven Tephra from the AD 260 eruption of Ilopango caldera. In P. D. Sheets (Ed.), *Archeology and Volcanism in Central America—The Zapotitán Valley of El Salvador* (pp. 15–34). Austin, TX: University of Texas Press.

Hartung, E., Caricchi, L., Floess, D., Wallis, S., Harayama, S., Kouzmanov, K., & Chiaradia, M. (2017). Evidence for residual melt extraction in the Takidani Pluton, Central Japan. *Journal of Petrology*, *58*, 763–788. https://doi.org/10.1093/petrology/egx033

Hernández, W. (2004). Caracterización Geotécnica y Vulcanológica de las Tefras Tierra Blanca Joven de la Caldera de Ilopango, El Salvador (Vol. 117). Universidad Politécnica.

Hernández, W., Ferrés, D., Delgado-Granados, H., Pullinger, C., Gutiérrez, D., & HEnríquez, E. (2010). The lat 40 ka eruptive cycle of Ilopango caldera deposits: A settlement for the San Salvador Metropolitan Area (El Salvador). In *International Conference Cities on Volcanoes, Fundación Canaria ITER, Tenerife* (Vol. 56).

Hernández, W., & Jicha, B. (2019). Múltiple colapso sectorial del volcán de San Salvador, El Salvado, América Central. *Revista de la Universidad Tecnológica de El Salvador* (Vol. 86, p. 74). ISBN 878-99961-86-17-2. 1a edición.

Holness, M. B. (2018). Melt segregation from silicic crystal mushes: A critical appraisal of possible mechanisms and their microstructural record. *Contributions to Mineralogy and Petrology*, *173*, 48. https://doi.org/10.1007/s00410-018-1465-2

Houghton, B., White, J. D. L., & Van Eaton, A. R. (2015). Phreatomagmatic and related eruption styles. In *The Encyclopedia of Volcanoes* (pp. 537–552). Elsevier. https://doi.org/10.1016/b978-0-12-385938-9.00030-4

Karakas, O., Degruyter, W., Bachmann, O., & Dufek, J. (2017). Lifetime and size of shallow magma bodies controlled by crustal-scale magmatism. *Nature Geoscience*, *10*, 446–450. https://doi.org/10.1038/ngeo2959

Keller, C. B., Schoene, B., & Samperton, K. M. (2018). A stochastic sampling approach to zircon eruption age interpretation. *Geochemical Perspectives Letters*, *8*, 31–35.

Kent, A. J. R., & Cooper, K. M. (2017). How well do zircons record the thermal evolution of magmatic systems? *Geology*, *46*, 111–114. https://doi.org/10.1130/g39690.1

Koch, A. J., & Mclean, H. (1975). Pleistocene tephra and ash-flow deposits in the volcanic highlands of Guatemala. *Geological Society of America Bulletin*, *86*, 529–541. https://doi.org/10.1130/0016-7606(1975)86<529:PTAADI>2.0.CO;2

Kutterolf, S., Freundt, A., & Perez, W. (2008). Pacific offshore record of Plinian arc volcanism in Central America: 2. Tephra volumes and erupted masses. *Geochemistry, Geophysics, Geosystems*, *9*, Q02S02. https://doi.org/10.1029/2007GC001791

Kutterolf, S., Freundt, A., Perez, W., Mörz, T., Schacht, U., Wehrmann, H., & Schmincke, H. U. (2008). Pacific offshore record of Plinian arc volcanism in Central America: 1. Along-arc correlations. *Geochemistry, Geophysics, Geosystems*, *9*, Q02S01. https://doi.org/10.1029/2007GC001631

Lücke, O. H. (2014). Moho structure of Central America based on three-dimensional lithospheric density modeling of satellite-derived gravity data. *International Journal of Earth Sciences*, *103*, 1733–1745. https://doi.org/10.1007/s00531-012-0787-y

Le Maitre, R. W., Bateman, P., Dudek, A., Keller, J., Lameyre, J., & Le Bas, M. (1989). A classification of igneous rocks and glossary of terms: Recommendations of the International Union of Geological Sciences Subcommission on the Systematics of Igneous Rocks. Blackwell Oxford.

Lexa, J., Sebesta, J., Chavez, J. A., Hernández, W., & Pecskay, Z. (2011). Geology and volcanic evolution in the southern part of the San Salvador Metropolitan Area. *Journal of Geosciences*, *56*, 106–140

Mahood, G. A. (1990). Second reply to comment of R.S.J. Sparks, H.E. Huppert and C.J.N. Wilson on "Evidence for long residence times of rhyolitic magma in the Long Valley magmatic system: The isotopic record in the precaldera lavas of Glass Mountain". *Earth and Planetary Science Letters*, *99*, 395–399. https://doi.org/10.1016/0012-821x(90)90145-n

Mann, C. P., Stix, J., Vallance, J. W., & Richer, M. (2004). Subaqueous intracaldera volcanism, Ilopango Caldera, El Salvador, Central America. In W. I. Rose, J. J. Bommer, D. L. López, M. J. Carr, & J. J. Major (Eds.), *Natural hazards in El Salvador* (Vol. 375, pp. 159–174). Boulder, CO: Geological Society of America Special Paper.

Mann, H. B., & Whitney, D. R. (1947). On a test of whether one of two random variables is stochastically larger than the other. *Annals of Mathematical Statistics*, *18*, 50–60. https://doi.org/10.1214/aoms/1177730491

McKenzie, D. (2011). Compaction and crystallization in magma chambers: Towards a model of the Skaergaard intrusion. *Journal of Petrology*, *52*(5), 905–930. https://doi.org/10.1093/petrology/egr009

Mehringer, P. J., Jr., Sarna-Wojcicki, A. M., Wollwage, L. K., & Sheets, P. (2005). Age and extent of the Ilopango TBJ Tephra inferred from a Holocene chronostratigraphic reference section, Lago De Yojoa, Honduras. *Quaternary Reserach*, *63*, 199–205. https://doi.org/10.1016/j.yqres.2004.09.011

Miller, C. F., & Wark, D. A. (2008). Supervolcanoes and their explosive supereruptions. *Elements*, *4*, 11–15. https://doi.org/10.2113/gselements.4.1.11

Miller, J. S., & Wooden, J. L. (2004). Residence, resorption and recycling of zircons in Devils Kitchen rhyolite, Coso Volcanic field, California. *Journal of Petrology*, *45*, 2155–2170. https://doi.org/10.1093/petrology/egh051

Newhall, C., Self, S., & Robock, A. (2018). Anticipating future Volcanic Explosivity Index (VEI) 7 eruptions and their chilling impacts. *Geosphere*, *14*, 572–603. https://doi.org/10.1130/ges01513.1

Newhall, C. G., & Dzurisin, D. (1988). *Historical unrest at the large calderas of the world*. Denver, CO: Department of the Interior, US Geological Survey.

Pedrazzi, D., Sunye-Puchol, I., Aguirre-Díaz, G., Costa, A., Smith, V. C., Poret, M., et al. (2019). The Ilopango Tierra Blanca Joven (TBJ) eruption, El Salvador: Volcano-stratigraphy and physical characterization of the major Holocene event of Central America. *Journal of Volcanology and Geothermal Research*, *377*, 81–102. https://doi.org/10.1016/j.jvolgeores.2019.03.006

Reid, M. R., & Coath, C. D. (2000). In situ U-Pb ages of zircons from the Bishop Tuff: No evidence for long crystal residence times. *Geology*, *28*, 443–446. https://doi.org/10.1130/0091-7613(2000)028<0443:ISUPAO>2.3.CO;2

Reid, M. R., Coath, C. D., Mark Harrison, T., & McKeegan, K. D. (1997). Prolonged residence times for the youngest rhyolites associated with Long Valley Caldera: 230Th-238U ion microprobe dating of young zircons. *Earth and Planetary Science Letters*, *150*, 27–39. https://doi.org/10.1016/s0012-821x(97)00077-0

Reid, M. R., & Vazquez, J. A. (2017). Fitful and protracted magma assembly leading to a giant eruption, Youngest Toba Tuff, Indonesia. *Geochemistry, Geophysics, Geosystems*, *18*, 156–177. https://doi.org/10.1002/2016GC006641

Richer, M., Mann, C. P., & Stix, J. (2004). Mafic magma injection triggers eruption at Ilopango caldera, El Salvador, Central America. In W. I. Rose, J. J. Bommer, D. L. López, M. J. Carr, & J. J. Major (Eds.), *Natural hazards in El Salvador* (Vol. 375, pp. 175–189). Boulder, CO: Geological Society of America Special Paper.

Ridolfi, F., Renzulli, A., & Puerini, M. (2010). Stability and chemical equilibrium of amphibole in calc-alkaline magmas: An overview, new thermobarometric formulations and application to subduction-related volcanoes. *Contributions to Mineralogy and Petrology*, *160*, 45–66. https://doi.org/10.1007/s00410-009-0465-7

Rivera, T. A., Schmitz, M. D., Jicha, B. R., & Crowley, J. L. (2016). Zircon petrochronology and 40Ar/39Ar sanidine dates for the Mesa Falls Tuff: Crystal-scale records of magmatic evolution and the short lifespan of a large Yellowstone magma chamber. *Journal of Petrology*, *57*, 1677–1704.

Rose, W. I., Conway, F. M., Pullinger, C. R., Deino, A., & McIntosh, W. C. (1999). An improved age framework for late Quaternary silicic eruptions in northern Central America. *Bulletin of Volcanology*, *61*, 106–120. https://doi.org/10.1007/s004450050266

Sambridge, M. S., & Compston, W. (1994). Mixture modeling of multi-component data sets with application to ion-probe zircon ages. *Earth and Planetary Science Letters*, *128*, 373–390. https://doi.org/10.1016/0012-821x(94)90157-0

Sánchez, I. A. E. (2015). *Levantamiento batimétrico y medición de parámetros fisicoquímicos del lago Ilopango, El Salvador*. Universidad de El Salvador.

Saxby, J., Gottsmann, J., Cashman, K., & Gutiérrez, E. (2016). Magma storage in a strike-slip caldera. *Nature Communications*, *7*, 1–10. https://doi.org/10.1038/ncomms12295

Scarlato, P., Mollo, S., Del Bello, E., von Quadt, A., Brown, R. J., Gutierrez, E., et al. (2017). The 2013 eruption of Chaparrastique volcano (El Salvador): Effects of magma storage, mixing, and decompression. *Chemical Geology*, *448*, 110–122. https://doi.org/10.1016/j.chemgeo.2016.11.015

Schindlbeck, J. C., Kutterolf, S., Freundt, A., Eisele, S., Wang, K. L., & Frische, M. (2018). Miocene to holocene marine tephrostratigraphy offshore Northern Central America and Southern Mexico: Pulsed activity of known volcanic complexes. *Geochemistry, Geophysics, Geosystems*, *19*, 4143–4173. https://doi.org/10.1029/2018GC007832

Schmitt, A. K. (2011). Uranium series accessory crystal dating of magmatic processes. *Annual Review of Earth and Planetary Sciences*, *39*, 321–349. https://doi.org/10.1146/annurev-earth-040610-133330

Schmitt, A. K., Grove, M., Harrison, T. M., Lovera, O., Hulen, J., & Walters, M. (2003). The Geysers-Cobb Mountain Magma System, California (Part 2): timescales of pluton emplacement and implications for its thermal history. *Geochimica et Cosmochimica Acta*, *67*(18), 3443–3458.

Schmitt, A. K., Stockli, D. F., Lindsay, J. M., Robertson, R., Lovera, O. M., & Kislitsyn, R. (2010). Episodic growth and homogenization of plutonic roots in arc volcanoes from combined U-Th and (U-Th)/He zircon dating. *Earth and Planetary Science Letters*, *295*, 91–103. https://doi.org/10.1016/j.epsl.2010.03.028

Self, S., & Blake, S. (2008). Consequences of explosive supereruptions. *Elements*, *4*, 41–46. https://doi.org/10.2113/gselements.4.1.41

Sheets, P. (2015). Volcanoes, ancient people, and their societies. In H. Sigurdsson, B. Houghton, S. McNutt, H. Rymer & J. Stix (Eds.), *The encyclopedia of volcanoes* (pp. 1313–1319).Elsevier. https://doi.org/10.1016/b978-0-12-385938-9.00076-6

Sliwinski, J. T., Bachmann, O., Dungan, M. A., Huber, C., Deering, C. D., Lipman, P., et al. (2017). Rapid pre-eruptive thermal rejuvenation in a large silicic magma body: The case of the Masonic Park Tuff, Southern Rocky Mountain volcanic field, CO, USA. *Contributions to Mineralogy and Petrology*, *172*, 30. https://doi.org/10.1007/s00410-017-1351-3

Smith, V. C., Costa, A., Aguirre-Díaz, G., Pedrazzi, D., Scifo, A., Plunkett, G., et al. (2020). The magnitude and impact of the 431 CE Tierra Blanca Joven eruption of Ilopango, El Salvador. *Proceedings of the National Academy of Sciences of the United States of America*, *117*(42), 26061–26068.

Spera, F. (1980). Thermal evolution of plutons: A parameterized approach. *Science*, *207*, 299–301. https://doi.org/10.1126/science.207.4428.299

Storm, S., Shane, P., Schmitt, A. K., & Lindsay, J. M. (2011). Contrasting punctuated zircon growth in two syn-erupted rhyolite magmas from Tarawera volcano: Insights to crystal diversity in magmatic systems. *Earth and Planetary Science Letters*, *301*, 511–520. https://doi.org/10.1016/j.epsl.2010.11.034

Storm, S., Shane, P., Schmitt, A. K., & Lindsay, J. M. (2012). Decoupled crystallization and eruption histories of the rhyolite magmatic system at Tarawera volcano revealed by zircon ages and growth rates. *Contributions to Mineralogy and Petrology*, *163*, 505–519. https://doi.org/10.1007/s00410-011-0682-8

Suñe-Puchol, I., Aguirre-Díaz, G. J., Dávila-Harris, P., Miggins, D. P., Pedrazzi, D., Costa, A., et al. (2019a). The Ilopango caldera complex, El Salvador: Origin and early ignimbrite-forming eruptions of a graben/pull-apart caldera structure. *Journal of Volcanology and Geothermal Research*, *371*, 1–19. https://doi.org/10.1016/j.jvolgeores.2018.12.004

Suñe-Puchol, I., Aguirre-Díaz, G. J., Pedrazzi, D., Dávila-Harris, P., Miggins, D. P., Costa, A., et al. (2019b). The Ilopango caldera complex, El Salvador: Stratigraphic revision of the complete eruptive sequence and recurrence of large explosive eruptions. *Journal of Volcanology and Geothermal Research*, *374*, 100–119. https://doi.org/10.1016/j.jvolgeores.2019.02.011

Valley, J. W. (2003). Oxygen isotopes in zircon. *Reviews in Mineralogy and Geochemistry*, *53*, 343–385. https://doi.org/10.2113/0530343

Vazquez, J. A., & Reid, M. R. (2002). Time scales of magma storage and differentiation of voluminous high-silica rhyolites at Yellowstone caldera, Wyoming. *Contributions to Mineralogy and Petrology*, *144*, 274–285. https://doi.org/10.1007/s00410-002-0400-7

Vazquez, J. A., & Reid, M. R. (2004). Probing the accumulation history of the voluminous Toba magma. *Science*, *305*, 991–994. https://doi.org/10.1126/science.1096994

Watson, E. B., & Harrison, T. M. (1983). Zircon saturation revisited: Temperature and composition effects in a variety of crustal magma types. *Earth and Planetary Science Letters*, *64*, 295–304. https://doi.org/10.1016/0012-821x(83)90211-x

Wilson, C. J. N., Houghton, B. F., Kampt, P. J. J., & McWilliamst, M. O. (1995). An exceptionally widespread ignimbrite with implications for pyroclastic flow emplacement. *Nature*, *378*, 605. https://doi.org/10.1038/378605a0

Wotzlaw, J.-F., Bindeman, I. N., Stern, R. A., D'Abzac, F.-X., & Schaltegger, U. (2015). Rapid heterogeneous assembly of multiple magma reservoirs prior to Yellowstone supereruptions. *Scientific Reports*, *5*, 14026. https://doi.org/10.1038/srep14026

Wotzlaw, J.-F., Bindeman, I. N., Watts, K. E., Schmitt, A. K., Caricchi, L., & Schaltegger, U. (2014). Linking rapid magma reservoir assembly and eruption trigger mechanisms at evolved Yellowstone-type supervolcanoes. *Geology*, *42*(9):807–810.

Zhang, B., Hu, X., Asimow, P. D., Zhang, X., Xu, J., Fan, D., & Zhou, W. (2019). Crystal size distribution of amphibole grown from hydrous basaltic melt at 0.6–2.6 GPa and 860–970°C. *American Mineralogist*, *104*, 525–535. https://doi.org/10.2138/am-2019-6759

References From the Supporting Information

Ball, L., Sims, K. W. W., & Schwieters, J. (2008). Measurement of234U/238U and230Th/232Th in volcanic rocks using the Neptune MC-ICP-MS. *Journal of Analytical Atomic Spectrometry*, *23*, 173–180. https://doi.org/10.1039/b703193a

Bell, E. A., Boehnke, P., Barboni, M., & Harrison, T. M. (2019). Tracking chemical alteration in magmatic zircon using rare earth element abundances. *Chemical Geology*, *510*, 56–71. https://doi.org/10.1016/j.chemgeo.2019.02.027

Friedrichs, B., Schmitt, A. K., McGee, L., & Turner, S. (2020). U-Th whole rock data and high spatial resolution U-Th disequilibrium and U-Pb zircon ages of Mt. Erciyes and Mt. Hasan Quaternary stratovolcanic complexes (Central Anatolia). *Data in Brief*, *29*, 105113. https://doi.org/10.1016/j.dib.2020.105113

Jarosewich, E., Nelen, J. A., & Norberg, J. A. (1980). Reference samples for electron microprobe analysis. *Geostandards Newsletter*, *4*, 43–47. https://doi.org/10.1111/j.1751-908x.1980.tb00273.x

Jochum, K. P., Nohl, U., Herwig, K., Lammel, E., Stoll, B., & Hofmann, A. W. (2005). GeoReM: A new geochemical database for reference materials and isotopic standards. *Geostandards and Geoanalytical Research*, *29*, 333–338. https://doi.org/10.1111/j.1751-908x.2005.tb00904.x

Kuehn, S. C., Froese, D. G., & Shane, P. A. R. (2011). The INTAV intercomparison of electron-beam microanalysis of glass by tephrochronology laboratories: Results and recommendations. *Quaternary International*, *246*, 19–47. https://doi.org/10.1016/j.quaint.2011.08.022

Norman, M. D., Pearson, N. J., Sharma, A., & Griffin, W. L. (1996). Quantitative analysis of trace elements in geological materials by laser ablation ICPMS: Instrumental operating conditions and calibration values of NIST glasses. *Geostandards Newsletter*, *20*, 247–261. https://doi.org/10.1111/j.1751-908x.1996.tb00186.x

Pearce, N. J. G., Perkins, W. T., Westgate, J. A., Gorton, M. P., Jackson, S. E., Neal, C. R., & Chenery, S. P. (1997). A compilation of new and published major and trace element data for NIST SRM 610 and NIST SRM 612 glass reference materials. *Geostandards Newsletter*, *21*(1), 115–144. https://doi.org/10.1111/j.1751-908x.1997.tb00538.x

Schindlbeck, J. C., Kutterolf, S., Freundt, A., Alvarado, G. E., Wang, K.-L., Straub, S. M., et al. (2016). Late Cenozoic tephrostratigraphy offshore the southern Central American Volcanic Arc: 1. Tephra ages and provenance. *Geochemistry, Geophysics, Geosystems*, *17*, 4641–4668. https://doi.org/10.1002/2016GC006503

Scott, S. R., Sims, K. W. W., Reagan, M. K., Ball, L., Schwieters, J. B., Bouman, C., et al. (2019). The application of abundance sensitivity filters to the precise and accurate measurement of uranium series nuclides by plasma mass spectrometry. *International Journal of Mass Spectrometry*, *435*, 321–332. https://doi.org/10.1016/j.ijms.2018.11.011

Sims, K. W., Hart, S., Reagan, M., Blusztajn, J., Staudigel, H., Sohn, R., et al. (2008a). ^{238}U-^{230}Th-^{226}Ra-^{210}Pb-^{210}Po, ^{232}Th-^{228}Ra, and ^{235}U-^{231}Pa constraints on the ages and petrogenesis of Vailulu'u and Malumalu Lavas, Samoa. *Geochemistry, Geophysics, Geosystems*, *9*, Q04003. https://doi.org/10.1029/2007GC001651

Sims, K. W. W., Gill, J. B., Dosseto, A., Hoffmann, D. L., Lundstrom, C. C., Williams, R. W., et al. (2008b). An Inter-Laboratory Assessment of the Thorium Isotopic Composition of Synthetic and Rock Reference Materials. *Geostandards and Geoanalytical Research*, *32*, 65–91. https://doi.org/10.1111/j.1751-908x.2008.00870.x

Szymanowski, D., Wotzlaw, J.-F., Ellis, B. S., Bachmann, O., Guillong, M., & von Quadt, A. (2017). Protracted near-solidus storage and pre-eruptive rejuvenation of large magma reservoirs. *Nature Geoscience*, *10*, 777. https://doi.org/10.1038/ngeo3020

van Achterberg, E., Ryan, C. G., Jackson, S. E., & Griffin, W. (2001). LA-ICP-MS in the Earth Sciences—Appendix 3, data reduction software for LA-ICP-MS. In P. J. Sylvester (Ed.), *Short course* (pp. 239–243). Quebec:Mineralogical Association of Canada.